Generating the 30-m land surface temperature product over continental China and USA from landsat 5/7/8 data

Jie Cheng [a,b,*], Xiangchen Meng [c,**], Shengyue Dong [a,b], Shunlin Liang [d]

[a] *State Key Laboratory of Remote Sensing Science, Beijing Normal University, Beijing, 100875, China*
[b] *Institute of Remote Sensing Science and Engineering, Faculty of Geographical Science, Beijing Normal University, Beijing, 100875, China*
[c] *College of Geography and Tourism, Qufu Normal University, Rizhao, 276826, China*
[d] *Department of Geographical Science, University of Maryland, College Park, 20742, USA*

A B S T R A C T

Generating a long-time-series, high-spatial-resolution land surface temperature (LST) product has considerable applications in monitoring water stress, surface energy and water balance at the field scale. This paper proposes an operational method to generate 30-m LSTs from thermal infrared (TIR) observations of Landsat series. Two key issues were addressed in the proposed method: one involved determining the land surface emissivity (LSE) by developing different LSE retrieval methods for specific land cover types; the other involved choosing an optimal reanalysis atmospheric profile for implementing the atmospheric correction of TIR data. After LSE determination and atmospheric correction, LST was resolved by inverting the radiative transfer equation. In situ measured LST and LSE data were used to validate the proposed method. The validation results based on the measurements from 24 sites showed that the absolute average bias of the LSE data estimated from Landsat 5/7/8 was generally within 0.01, and the standard deviations were all less than 0.002. The average biases of the retrieved LST at SURFRAD sites were 1.11/1.54/1.63 K, whereas the RMSEs were 2.72/3.21/3.02 K for Landsat 5/7/8, respectively. The average biases (RMSEs) of the retrieved LST at the BSRN and Huailai sites were 0.08 K (3.69 K) and 0.90 K (3.42 K) for Landsat 7 and Landsat 8, respectively. Furthermore, the validation results at the SURFRAD sites show that the precision and uncertainty of the retrieved Landsat 5/7/8 LSTs were all better than those of the USGS LSTs. Finally, we produced monthly composited LST maps for the Chinese landmass and continental United States using the retrieved Landsat 5/7/8 LSTs. This study provides guidance on how to estimate large-scale LSTs from satellite sensors with only one TIR channel. We will massively produce global LSTs from Landsat series TIR data and release them to the public in the next stage.

1. Introduction

The land surface temperature (LST) plays an important role in the interactions and all energy exchanges between the atmosphere and land surface (Cheng et al., 2020; Coll et al., 2016; Li et al., 2013b; Meng and Cheng 2020; Wan and Dozier 1996). It is a key parameter in models of the surface radiation budget, energy balance, and water circulation on regional and global scales (Tang et al., 2017; Trigo et al., 2008; Yu et al., 2009). At present, LST can be obtained by ground measurement, remote sensing, and land surface modeling (Ouyang et al., 2018). Due to sparsely distributed ground measurement sites and inaccurate model simulations, it is almost impossible to effectively monitor LST with

spatiotemporal continuity; remote sensing is an irreplaceable way to obtain LST at the global and regional scale (Xu and Cheng 2021).

Currently, LST is primarily estimated from passive microwave sensors and thermal infrared (TIR) sensors. Moreover, a few operational LST products with different spatial and temporal resolutions have been produced using various sensors, such as the spinning enhanced visible and infrared imager (SEVIRI) (Niclòs et al., 2011), moderate resolution imaging spectro-radiometer (MODIS) (Wan 2014), advanced space-borne thermal emission and reflection radiometer (ASTER) (Gillespie et al., 1998), visible infrared imaging radiometer suite (VIIRS) (Yu et al., 2005), medium resolution spectral imager (MERSI) (Meng et al., 2017), and advanced microwave scanning radiometer (AMSR-E) (Zhang and

Cheng 2020).

However, the spatial resolution of most LST products is relatively low and cannot meet the requirements of applications such as water stress, fire monitoring and evapotranspiration estimation at the field scale (Sobrino et al., 2016). Therefore, generating LST products with a high spatial resolution has considerable potential for these applications.

Landsat series satellites provide a long period of data records (more than 40 years) (Anderson et al., 2012; Cheng et al., 2017c; Wulder et al., 2016). Thermal infrared observations from the Landsat series are a valuable data source for obtaining long-term high spatial resolution LST records. However, the Landsat TIR data were previously ignored until the development of the LST retrieval algorithms for Landsat Thematic Mapper (TM) data (Jiménez-Muñoz and Sobrino 2003; Qin et al., 2001). Since then, many algorithms have emerged, such as bamboo shoots after rain. These algorithms can be categorized into single-channel algorithms (Jiménez-Muñoz and Sobrino 2003; Malakar et al., 2018; Qin et al., 2001), split-window (SW) algorithms (Jiménez-Muñoz et al., 2014; Meng et al., 2019; Rozenstein et al., 2014), and other algorithms (Saradjian and Jouybari-Moghaddam 2019; Zhang et al., 2019). Except for the Landsat 8 satellite, Landsat series satellites carry only one TIR sensor; therefore, only single-channel algorithms can be used for retrieving LST. Moreover, due to the large calibration uncertainty in Landsat 8 Thermal Infrared Sensor (TIRS) channel 11, it is not recommended to use SW algorithms to retrieve LST (Malakar et al., 2018). Therefore, single-channel algorithms were used as the consistent LST retrieval algorithm to estimate LST from Landsat series TIR data.

Single-channel algorithms mainly include the mono window (MW) algorithm (Qin et al., 2001), the generalized single-channel (GSC) method (Jiménez-Muñoz and Sobrino 2003), and the radiative transfer equation (RTE) method (Malakar et al., 2018). Qin et al. developed the MW algorithm for LST retrieval from Landsat TM6 data, where emissivity, transmittance and effective mean atmospheric temperature are required as the input parameters (Qin et al., 2001). Wang et al. proposed an improved MW algorithm for Landsat 8 TIRS channel 10 data and used meteorological data to calculate the effective mean atmospheric temperature. The evaluation results using simulation data showed that the improved MW algorithm has an average deviation of 0.67 K and a root mean square error (RMSE) of 0.43 K (Wang et al., 2015a). Jiménez-Muñoz and Sobrino developed the GSC method for retrieving LST from only one TIR channel and can be applied to TM6 data (Jiménez-Muñoz and Sobrino 2003). Evaluation results using independent simulated data indicated that when the atmospheric water vapor content was lower than 2 g/cm^2, RMSE values were below 1 K in most cases. However, when the atmospheric water vapor content is higher than 3 g/cm^2, errors are unacceptable (Jiménez-Muñoz et al., 2009). Jiménez-Muñoz et al. applied the GSC method to Landsat 8 TIR data using the refitted coefficients calculated from the Global Atmospheric Profiles from the Reanalysis Information (GAPRI) profile, with a mean error below 1.5 K tested using simulated data (Jiménez-Muñoz et al., 2014). Cristóbal et al. developed an improved GSC method that can be applied to Landsat series satellites, which needs near-surface air temperature and atmospheric water vapor content as input data (Cristóbal et al. 2009, 2018). The improved GSC method provided better performance than the GSC method and yielded overall errors of approximately 1 K and a bias of −0.5 K (Cristóbal et al., 2018). The RTE method was used by Cook et al. to retrieve LSTs from Landsat 8 TIRS channels 10 and 11, and the validation results showed that the mean errors (standard deviations (STDs)) of LSTs under cloudless conditions were −0.56 K (0.76 K) and −2.16 K (1.64 K), respectively (Cook et al., 2014). Landsat 5 and 7 LST products in the United States were produced by Malakar et al. using the RTE method. Compared with the measured data at the SURFRAD site, the mean biases (RMSEs) of the Landsat 5 and 7 LST products are 0.7 K (2.2 K) and 0.9 K (2.3 K), respectively (Malakar et al., 2018). Besides, researchers also compared the accuracy of retrieved LST using different algorithms and emissivity models(Sekertekin and Bonafoni 2020; Yu et al., 2014).

Although a few of these algorithms have been widely used for retrieving LST from Landsat series TIR data, there are still some problems that need to be resolved. First, the empirical formula for calculating the effective mean atmospheric temperature required in the MW algorithm may not be suitable for some special study areas (Zhou et al., 2010). Second, the empirical relationship used for estimating the land surface emissivity (LSE) over nonvegetated surfaces was fitted by using the emissivity spectra from the spectral library (Baldridge et al., 2009). The limited amount of spectral library data cannot represent the complex global situation. Third, although ground measurements have been widely used to validate the derived Landsat LST (Sekertekin 2019; Sekertekin and Bonafoni 2020; Zhang et al., 2016), the current algorithms and validations are mainly focusing on the Landsat 8 data and the exploration of historical Landsat 5 and 7 data is still insufficient. Furthermore, although the U.S. Geological Survey (USGS) has recently released the global Landsat LST product, the product has not been extensively validated.

This study aims to develop an operational LST retrieval method for generating long-term 30 m LST products from Landsat series data by addressing two key issues in the retrieval of LST from one-channel observations. The structure of the paper is arranged as follows: Section 2 introduces the data used in this study; Section 3 describes the methodology for LST retrieval; Section 4 and Section 5 presents the results and discussion of the accuracy of the retrieved Landsat LSE and LST; Section 6 shows the monthly composited LST maps at the country level; and the final section provides the conclusions of this study.

2. Data

2.1. Landsat series products

Since 1972, the USGS has produced, archived, and distributed Landsat satellite data. The Landsat TM, Enhanced Thematic Mapper Plus (ETM+), Operational Land Imager (OLI) and TIRS onboard the Landsat series satellites have acquired images of the Earth nearly continuously, with a 16-day repeat cycle. Detailed information about the Landsat series satellites can be found on page https://www.usgs.gov/core-science-systems/nli/landsat. In this paper, Landsat 5, 7 and 8 Collection 1 (C1) Level 1 (L1) and C1 Level 2 (L2) products were used to generate LST and were downloaded from https://earthexplorer.usgs.gov/. Fig. 1 shows the spectral response for channel 6 of Landsat 5/ TM, Landsat 7/ETM+ and channels 10 and 11 of Landsat 8/TIRS.

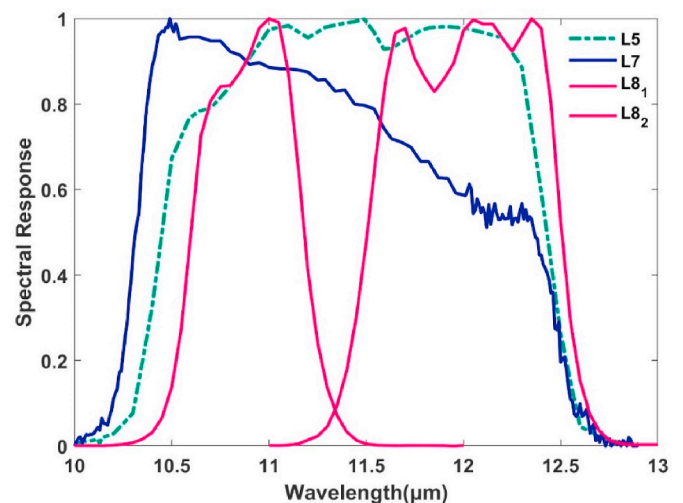Landsat C1 L1 products have consistent geometric and calibrated

Fig. 1. Spectral response functions for channel 6 of Landsat 5 (L5)/TM and Landsat 7 (L7)/ETM+ and channels 10 and 11 of Landsat 8/TIRS are denoted as L8$_1$ and L8$_2$, respectively.

radiometric qualities supported by metadata and per-pixel quality flags (Wulder et al., 2019). Landsat C1 L1 products consist of quantized and calibrated scaled digital numbers (DNs), which can be rescaled to top of atmosphere (TOA) reflectance and radiance using conversion co-efficients provided in the metadata file. Landsat C1 L2 products include the Landsat surface reflectance (SR) product. Landsat 5 and Landsat 7 SR products are derived from the Landsat Ecosystem Disturbance Adaptive Processing System (LEDAPS) (Masek et al., 2006), and Landsat 8 SR products are produced by the Landsat Surface Reflectance Code (LaSRC) algorithm (Vermote et al., 2016). Landsat SR products also contain pixel quality bands, saturation masks, and aerosol masks. Among these, the pixel quality band includes several tags, e.g., clear, water, snow, cloud, cloud shadow, etc. These tags are used in the subsequent LSE calculations and cloud mask.

2.2. Auxiliary data

2.2.1. MERRA2

The Modern-Era Retrospective analysis for Research and Applications version 2 (MERRA-2) is a NASA atmospheric reanalysis using the Goddard Earth Observing System Model, Version 5 (GEOS-5) data assimilation system version 5.12.4. MERRA-2 covers the period of 1980–present, and it continues to be an ongoing climate analysis product as resources allow (Meng and Cheng 2018). MERRA-2 data files are provided in netCDF-4 format. In this paper, M2I6NPANA (inst6_3d_ana_Np) data products were used for atmospheric correction of the TIR sensor aboard the Landsat series satellites, and this product can be accessed on the following website: https://search.earthdata.nasa.gov. The M2I6NPANA (hereafter MERRA2) is the analyzed meteorological field for 42 pressure levels (from the surface to 0.1 hPa). The spatial resolution is 0.625° longitude × 0.5° latitude, and the temporal resolution is 6 h, which means that a daily file contains data at 00, 06, 12, and 18 UTC.

2.2.2. ASTER LSE product

The ASTER land surface emissivity product (AST_05), retrieved by the classical temperature/emissivity separation (TES) algorithm (Gillespie et al., 1998), was downloaded from https://search.earthdata.nasa.gov/. The spatial resolution of AST_05 is 90 m, and the accuracy for five ASTER narrowband emissivities is within 0.015 (Gillespie et al., 1998) based on numerical simulation and field validation studies. According to scholars' research, AST_05 has been proven to be relatively accurate, and there is almost no seasonal variation in arid areas (Cheng et al., 2017a; Gillespie et al., 2011; Hulley and Hook 2009b; Sabol et al.,

2009). AST_05 along with the Landsat SR product was used to establish the empirical relationship between LSE and SR for nonvegetated surfaces.

2.2.3. Soil taxonomy data

The soil taxonomy data were distributed by the United States Department of Agriculture (USDA) (https://www.nrcs.usda.gov/). The data contain 5400*10800 grids with a spatial resolution of approximately 0.0333° (Cheng et al., 2014b). The data contain 12 soil types, rock and shifting sand, and the spatial distribution of each soil type is shown in Fig. 2. Based on this product, the training and testing data of different soil types can be selected on a global scale. As shown in the black box in Fig. 2, relatively large and homogeneous areas were selected as the study area for each soil type (Cheng and Liang 2014), which may improve the applicability of the algorithm.

2.2.4. MODIS land cover product

The MODIS Collection 6 Land Cover product (MCD12Q1) provides an annual land cover dataset with a 500-m spatial resolution for six classification schemes. The classification scheme included five classification schemes from MCD12Q1 Collection 5 (i.e., the International Geosphere-Biosphere Programme (IGBP) legend, the University of Maryland (UMD) legend, the Leaf Area Index and Fraction of Photosynthetically Active Radiation (LAI/FPAR) biome legend, the Biome-BGC model (BGC) legend, the Plant Functional Types (PFT) legend) and a new classification scheme based on the Land Cover Classification System (LCCS) from the Food and Agricultural Organization (FAO) (Sulla-Menashe et al., 2019). The IGBP classification scheme was selected as a reference to determine the leaf emissivity of vegetated surfaces.

2.3. Field measurements

2.3.1. LSE measurements

The ground-measured LSE comes from five sources, and detailed information can be found in Table 1. To validate the North American ASTER Land Surface Emissivity Database, Hulley et al., (2009) collected sand samples during the spring and early summer in 2008 and measured their directional-hemispherical reflectances in the laboratory using a Nicolet 520 Fourier transform infrared (FTIR) spectrometer equipped with a Labsphere integrating sphere. The directional emissivity was calculated using Kirchhoff's law. The ASTER channel emissivities were obtained by convolving the measured emissivity spectra with the ASTER TIR spectral response functions. Using the same method, Hulley and
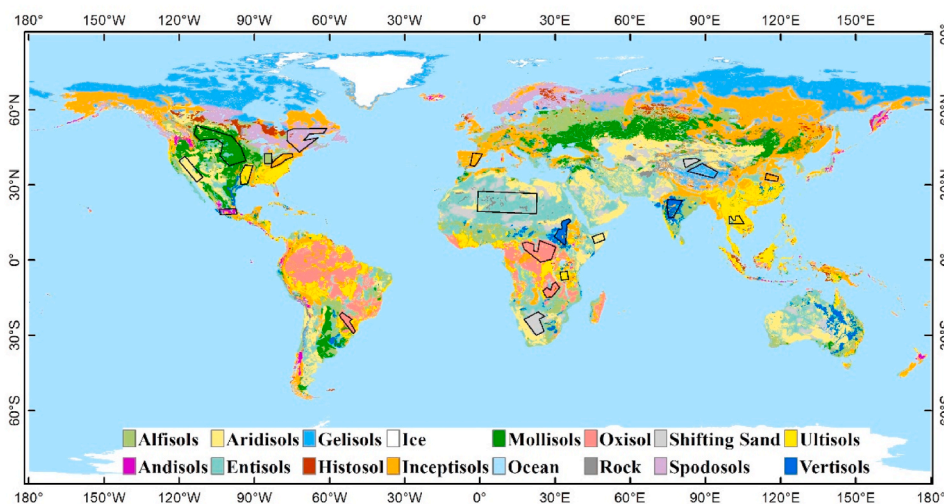

Fig. 2. The USDA soil taxonomy data and selected study areas (black boxes). Samples of soil types (Histosol and Rock) were not selected in the estimation of land surface emissivity.

Table 1
Detailed information on the derived-site emissivities for Landsat 5/7/8.

No.	Sites name	Location(lat,lon)	Referenced LSE				Path/Row	Measure time
			L5/b6	L7/b6	L8/b10	L8/b11		
1	Great Sands[a]	37.77,-105.54	0.9595	0.9500	0.9404	0.9698	033/034	Spring and early summer of 2008
2	WhiteSands[a]	32.89,-106.33	0.9787	0.9770	0.9768	0.9807	033/037	
3	Killpecker[a]	41.98,-109.10	0.9602	0.9487	0.9374	0.9726	036/031	
4	LittleSahara[a]	39.70,-112.39	0.9663	0.9591	0.9523	0.9743	038/032	
5	Kelso[a]	34.91,-115.73	0.9578	0.9473	0.9365	0.9694	039/036	
6	Algodones[a]	32.95,-115.07	0.9722	0.9662	0.9614	0.9788	039/037	
7	Stovepipe[a]	36.62,-117.11	0.9700	0.9639	0.9586	0.9767	040/035	
8	Moses Lake[a]	47.05,-119.31	0.9758	0.9709	0.9676	0.9811	044/027	
9	Kubuqi1 [e]	40.305,109.616	0.9664	0.9608	0.9543	0.9714	128/032	2015–10
10	Kubuqi2 [e]	40.460,108.692	0.9668	0.9614	0.9553	0.9715		
11	Wulanbuhe1 [e]	39.719,106.672	0.9663	0.9611	0.9553	0.9708	129/032	
12	Wulanbuhe2 [e]	39.879,106.642	0.9651	0.9591	0.9522	0.9704		
13	Tenggeli1 [e]	37.483,104.972	0.9664	0.9608	0.9543	0.9714	130/034	
14	Tenggeli2 [e]	37.493,104.962	0.966	0.9601	0.9532	0.9713		
15	Badanjilin2 [e]	39.756,102.326	0.9672	0.9621	0.9563	0.9717	132/032	2012–07
16	Badanjilin1[e]	39.499,102.381	0.9663	0.9611	0.9553	0.9708	132/033	
17	GeBi [d]	38.915, 100.304	0.9744	0.9721	0.9708	0.9770	133/033	
18	HuaZhaiZi [d]	38.765,100.319	0.9775	0.9751	0.9742	0.9801		
19	ShenShaWo1[d]	38.789, 100.493	0.9772	0.9703	0.9653	0.9847		
20	ShenShaWo2 [e]	38.789, 100.493	0.9686	0.9637	0.9584	0.9727		2015–10
21	Mingshashan [e]	40.083,94.679	0.9645	0.9588	0.9522	0.9697	137/032	
22	Taklimakan1[c]	38.97,83.57	0.9452	0.9414	0.9447	0.9463	144/033	2011–06
23	Taklimakan2[c]	38.97,83.69	0.9504	0.9447	0.9459	0.9541		
24	Namib[b]	−24.699,15.474	0.9724	0.9652	0.9583	0.9795	179/077	2008–07

[a] Represents the measurement site of (Hulley et al., 2009).
[b] Represents the measurement site of (Hulley and Hook 2009).
[c] Represents the measurement site of (Dong et al., 2013). [d] represents the measurement site of (Wang et al., 2015). [e] represents the measurement site of (Li et al., 2020).

Hook (2009a) obtained the emissivities of eight sand samples collected from the Namib Desert during July 2008 to validate V4, 4.1, and 5 of the MODIS land surface temperature and emissivity products.

Dong et al. validated the Global LAnd Surface Satellite (GLASS) broadband emissivity (BBE) by using field-measured emissivity spectra at two sites in the Taklimakan Desert, China, during June 2011 (Dong et al., 2013). In the field experiment, a portable FTIR spectrometer (Model 102F) equipped with a Labsphere gold plate was used to measure the surface emitted spectral radiance and gold plate reflected environmental radiation. The emissivity spectrum was derived by using the iterative spectrally smooth temperature-emissivity separation (ISSTES) algorithm (Borel 2008).

Wang et al. validated the ASTER LSE product by using field-measured emissivity of sand samples collected at three automatic meteorological stations (Shenshawo, Huazhaizi, and Gebi) in northwestern China on July 10, 2012 (Wang et al., 2015b). An ABB BOMEM MR304 FTIR spectroscope equipped with a diffuse golden plate was used to obtain the radiation of the surface and environment. The method for obtaining the emissivity is the same as that used by Dong et al., (2013).

Li et al. evaluated MODIS level-2 LST products (MYD11_L2 and MYD21_L2) over barren surfaces in northwestern China using temperature-based (T-based) and radiance-based (R-based) methods (Li et al., 2020). The directional-hemispherical reflectance of ten sand samples collected from six large deserts in northwestern China was measured in the laboratory using a Thermo Fisher iS50 FTIR spectrometer equipped with a Pike integrated sphere. The emissivity spectrum was calculated using Kirchhoff's law.

With the collected emissivity data mentioned above, we can derive the corresponding LSE of Landsat 5/7/8, as shown in Table 1. If the obtained emissivity is the emissivity spectrum, we directly convolved it with the spectral response functions of Landsat 5/7/8 to generate channel emissivities. Otherwise, we established the conversion formulae between Landsat 5/7/8 LSE and ASTER and MODIS channel LSE by using linear regression with the representative emissivity spectra from ASTER and MODIS spectral libraries.

2.3.2. Ground measured LST

The ground LST measurements were obtained from three sources, including the Surface Radiation Budget Network (SURFRAD, https:// www.esrl.noaa.gov/gmd/grad/surfrad/sitepage.html), Baseline Surface Radiation Network (BSRN, https://bsrn.awi.de/) and National Tibetan Plateau Data Center (NTPDC, https://data.tpdc.ac.cn/zh-hans/). The multiscale surface flux and meteorological observation datasets in the Haihe River Basin (Liu et al., 2013) in the NTPDC were used in this article. Twelve sites in total, including seven SURFRAD sites, four BSRN sites, and the Huailai site on the Haihe River (hereafter referred to as Huailai), were chosen to validate the estimated LST. These sites, especially the SURFRAD sites, have been widely used to validate LST products and surface longwave radiation products (Cheng et al., 2013; Duan et al., 2019; Guillevic et al., 2014; Malakar et al., 2018; Meng et al., 2019; Wang et al., 2020; Yu et al., 2009; Zeng et al., 2020). Specific information on each in situ site is shown in Table 2.

In situ LSTs were calculated from the site-measured surface longwave downward radiation and surface longwave upward radiation using the following equation:

$$T_s = \left[\frac{F^\uparrow - (1 - \varepsilon_b)F^\downarrow}{\varepsilon_b \sigma} \right]^{\frac{1}{4}} \tag{2}$$

where T_s is the surface LST, $F^\uparrow$ is the measured surface longwave upward radiation, $F^\downarrow$ is the measured surface longwave downward radiation, σ is Stefan–Boltzmann's constant (5.67×10^{-8} W/m²/K⁴), and ε_b is the BBE, which can be calculated from the in situ measured emissivity or the five ASTER spectral emissivities using the following equation (Cheng et al., 2013):

$$\varepsilon = 0.197 + 0.025\varepsilon_{10} + 0.057\varepsilon_{11} + 0.237\varepsilon_{12} + 0.333\varepsilon_{13} + 0.146\varepsilon_{14} \tag{3}$$

3. Methodology

Assuming that the land surface is Lambertian and ignoring solar irradiance, the radiative transfer equation (RTE) for thermal infrared is

Table 2
Detailed information on the selected sites and the corresponding Landsat 5/7/8 Path/Row.

	Site	Full Name	Latitude	Longitude	Land cover	Landsat period	Path/Row
SURFRAD	BND	Bondville	40.052	−88.373	cropland	2001–2019	023/032
	GWN	GoodwinCreek	34.255	−89.873	grassland	2001–2019	023/036
	PSU	Penn. State Univ.	40.720	−77.931	cropland	2001–2019	016/032
	SXF	Sioux Falls	43.734	−96.623	grassland	2003–2019	029/030
	FPK	Fort Peck	48.308	−105.102	grassland	2001–2019	035/026
	TBL	TableMountain	40.126	−105.238	grassland	2001–2019	033/032
	DRA	Desert Rock	36.623	−116.020	shrubland	2001–2019	040/035
HuaiLai	HL	HuaiLai	40.349	115.788	cropland	2013–2019	123/032
							124/032
BSRN	CAB	Cabauw	51.971	4.927	grassland	2013–2019	198/024
	GOB	Gobabeb	−23.561	15.042	desert	2012–2019	179/076
	PAY	Payerne	46.815	6.944	cropland	2013–2019	195/027
	TAT	Tateno	36.058	140.126	grassland	2013–2019	107/035

expressed as follows (Cheng et al., 2020):

$$L_i = \left[\varepsilon_i B_i(T_s) + (1 - \varepsilon_i) L_i^{\downarrow} \right] \tau_i + L_i^{\uparrow} \qquad (4)$$

where L_i is the at-sensor radiance of channel i, T_s is the LST, $B_i(T_s)$ is the blackbody radiance of channel i, ε_i is the LSE of channel i, and $L_i^{\uparrow}$, $L_i^{\downarrow}$ and τ_i are the atmospheric upward radiance, downward radiance and transmittance of channel i, respectively.

For sensors with only one TIR channel, such as Landsat 5/TM and Landsat 7/ETM+, LST can be calculated by providing LSE and three atmospheric parameters ($L_i^{\uparrow}$, $L_i^{\downarrow}$ and τ_i). In this article, the RTE algorithm is selected as the consistent LST retrieval algorithm for the Landsat series for two reasons: one is that large calibration uncertainty associated with TIR channel 11 has been identified by USGS; the other is that the RTE algorithm has the highest accuracy among single-channel algorithms, according to previous studies (Windahl and Beurs 2016; Yu et al., 2014). The overall flow chart for LST retrieval is shown in Fig. 3, including LSE estimation using the new scheme, atmospheric correction based on MERRA2 reanalysis data, and LST estimation based on the RTE algorithm.

3.1. Land surface emissivity estimation

A new scheme was proposed for estimating Landsat LSE in this article. The land surface was classified into four types: snow/ice, water, vegetated surfaces and nonvegetated surfaces, and their LSE was estimated separately. For snow/ice and water surfaces, the LSEs were set to constant values. The flow chart for generating LSEs for the remaining surface types is shown in Fig. 4. For the nonvegetated surfaces, the LSEs were estimated by using an empirical method that establishes the linkages between the ASTER LSE product and Landsat SR product. For the vegetated surfaces, the LSEs were derived by using the 4SAIL model lookup table (LUT) method provided with the LSE of the leaf emissivity, soil background, and leaf area index (LAI).

3.1.1. Nonvegetated surfaces

Surface optical variables (e.g., NDVI, FVC, reflectance, and spectral albedo) have been used to estimate TIR variables (LST and emissivity) (Griend and Owe 1993; Menenti et al., 1989; Sobrino et al., 2008) for a long time. Cheng et al. (2017b) demonstrated that there is a potential physical linkage between LSE and reflective variables with limited samples. Therefore, we established the empirical relationship between Landsat LSE and SR of visible, near-infrared and shortwave radiation.
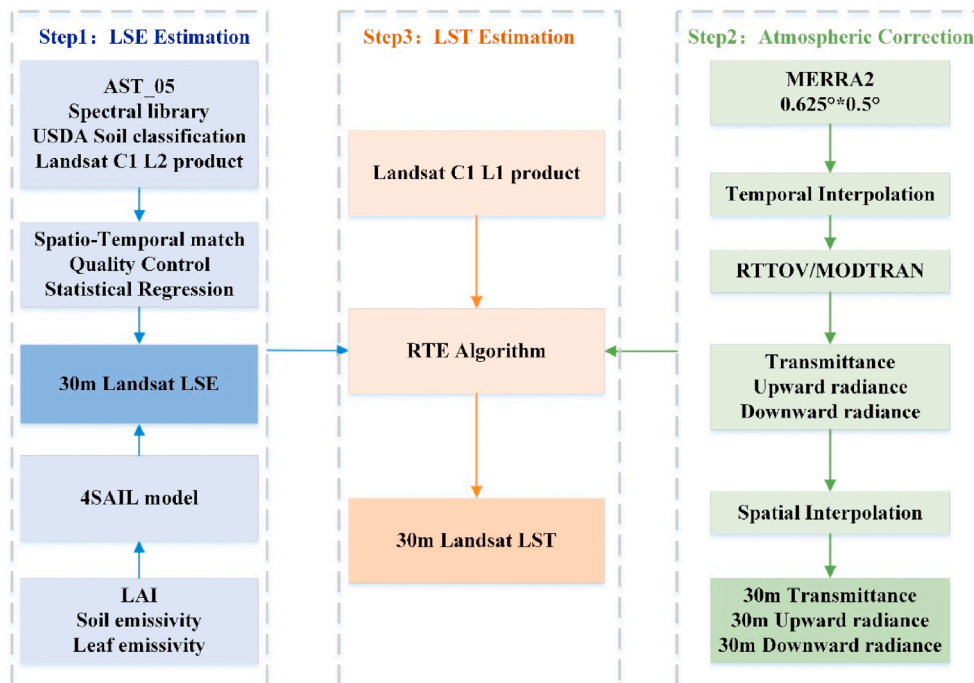

Fig. 3. Overall flow chart for generating 30 m land surface temperature from the observations of Landsat 5/7/8.
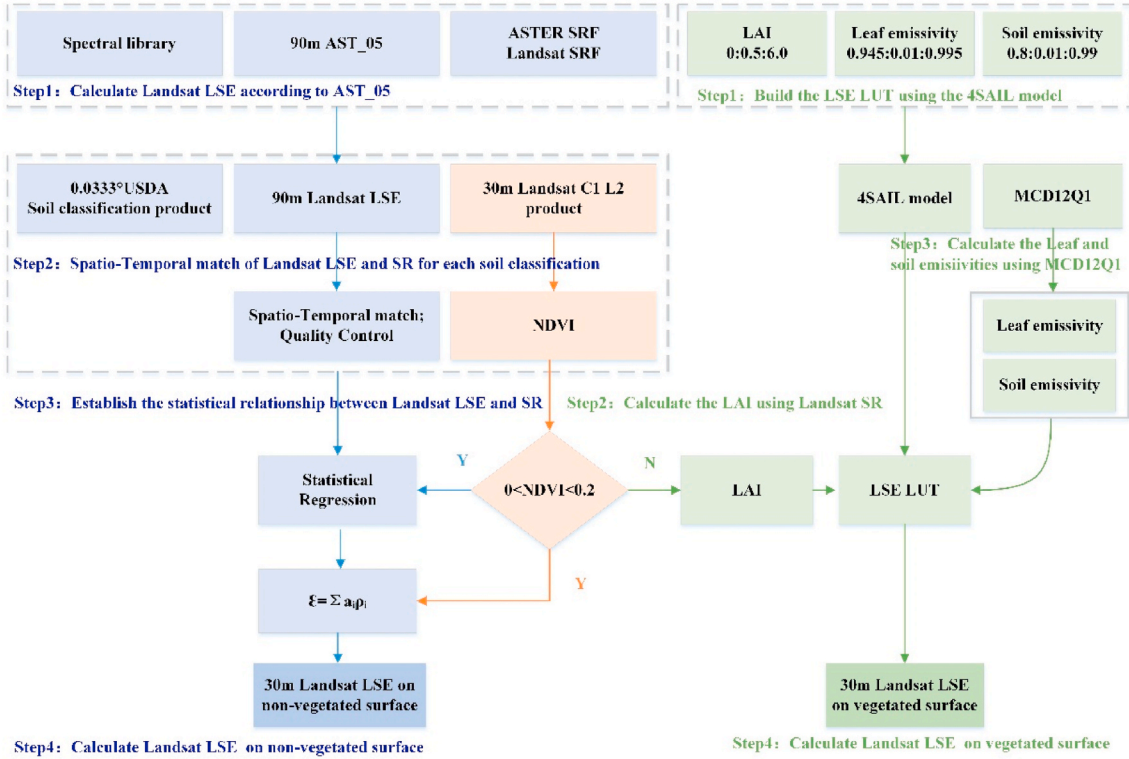
Fig. 4. Flow chart for generating Landsat land surface emissivity, excluding ice/snow and water.

$$\varepsilon_i = a_0 + \sum a_j * \rho_j \qquad (5)$$

where ε_i is the LSE of Landsat 5/7/8 TIR channel i, ρ_j is the SR of Landsat channels 1–7, a_0 is the constant term, and a_j is the coefficient corresponding to channel i. It is intuitive to fit the coefficients in Equation (5) using the spectral library data. However, the empirical relationship established from the limited samples in the spectral libraries may not fully characterize the temporal and spatial variation characteristics of real LSE at larger scales. Thus, we use the collocated ASTER LSE product and Landsat SR product acquired in different seasons to fit the coefficients, expecting to obtain a more accurate LSE estimate. The flow chart for estimating Landsat LSE over nonvegetated surfaces is shown in Fig. 4, which includes the following three aspects. (1) Spectral conversion. The LSE of Landsat TIR channels can be expressed as a linear combination of ASTER narrowband emissivities, and the regression coefficients were derived by combining ASTER/MODIS spectral library data and ASTER/Landsat spectral response functions. The regression equations are expressed as Equation (6). (2) Spatial-temporal match. Assuming that the LSE remains unchanged within one week, ASTER images that meet the time threshold (3 days before and after the overpass time of the Landsat satellite) are searched for. The nearest neighbor sampling method was used to obtain the matchups. The data quality control was divided into two steps. First, invalid pixels affected by clouds and cloud shadows were removed before the spatial-temporal match, according to the pixel quality bands of ASTER and Landsat. Second, the outliers that existed in the matched data were removed after the spatial-temporal match. The lower quartile (Q1), upper quartile (Q2) and interquartile range (IQR) of all matched data were calculated, and values that were less than Q1-1.5 IQR or greater than Q2+1.5 IQR were removed. (3) Statistical regression. If the Landsat NDVI is larger than 0 and less than 0.2, the empirical relationship between the ASTER emissivity and Landsat 5/7/8 SRs was established at a coarse resolution of ~90 m using the least square method. Assuming that this empirical relationship can be applied to 30 m spatial resolution, Landsat LSE data were estimated by inputting the Landsat 8 SR data.

$$\begin{aligned}
\varepsilon_{L5/b6} &= -0.147\varepsilon_{AST13} + 0.992\varepsilon_{AST14} + 0.153 \,,\; R^2 = 0.942,\; RMSE = 0.004 \\
\varepsilon_{L7/b6} &= 0.278\varepsilon_{AST13} + 0.599\varepsilon_{AST14} + 0.121 \,,\; R^2 = 0.975,\; RMSE = 0.003 \\
\varepsilon_{L8/b10} &= 0.636\varepsilon_{AST13} + 0.384\varepsilon_{AST14} - 0.018 \,,\; R^2 = 0.998,\; RMSE = 0.001 \\
\varepsilon_{L8/b11} &= -0.599\varepsilon_{AST13} + 1.404\varepsilon_{AST14} + 0.193 \,,\; R^2 = 0.892,\; RMSE = 0.005
\end{aligned}$$
$$(6)$$

3.1.2. Vegetated surfaces

Following the study of Cheng et al. (2016), we estimated the LSE over vegetated surfaces using a look-up table (LUT)-based method to improve the computing efficiency. The 4SAIL (Scattering by Arbitrarily Inclined Leaves) model (Verhoef et al., 2007) was used to establish the LUT, in which canopy LSE was determined by using the leaf emissivity, soil background emissivity, and LAI. In the model, the directional emissivity of the soil-canopy system can be expressed as (Cheng et al., 2016):

$$\varepsilon_o = \gamma_o + \frac{\tau_{do} + \tau_{oo}}{1 - r_s\rho_{dd}}r_s\gamma_d + \frac{\tau_{do} + \tau_{oo}}{1 - r_s\rho_{dd}}\varepsilon_s \qquad (7)$$

where ρ is the reflectance, τ is the transmittance of the isolated canopy layer, r_s is the reflectance of the Lambertian soil, and $\varepsilon_s = 1 - r_s$ is the soil emissivity. The double subscripts indicate the types of flux on incidence and exit, where s, d, and o denote solar hemispherical, diffuse hemispherical, and flux in the observer's direction, respectively. *dd*, *do* and *oo* represent bihemispherical, hemispherical-directional (in the viewing direction), and direct (transmittance) in the direction of observation, respectively.

The hemispherical emissivity γ_d and directional emissivity γ_o of the isolated canopy layer can be expressed as:

$$\begin{aligned}
\gamma_d &= 1 - \rho_{dd} - \tau_{dd} \\
\gamma_o &= 1 - \rho_{do} - \tau_{do} - \tau_{oo}
\end{aligned} \qquad (8)$$

The flow chart for generating Landsat LSE on vegetated surfaces is also shown in Fig. 4, and the main process can be divided into three steps:

(1) LUT with the 4SAIL model was constructed. The three principal model inputs were set as follows: leaf emissivity ranged from 0.945 to 0.995 with an interval of 0.01; soil emissivity varied from 0.80 to 0.99 with an interval of 0.01; and LAI ranged from 0 to 6.0 with an interval of 0.5.

(2) The input parameters of the LUT were determined. The emissivity data used to train the linear relationship in Section 3.1.1 were used to calculate the average values for different soil types. The calculated statistical emissivity values were set as the soil background values. If the Landsat NDVI is greater than or equal to 0.2, the Landsat NDVI along with the MCD12Q1 product were used to identify the vegetation pixels, and the predetermined leaf emissivity values were assigned to each vegetated surface type. Detailed information on the leaf and soil emissivity is shown in Tables 3 and 4.

Although researchers have proposed a large number of versatile algorithms for retrieving the LAI from Landsat images (Chen and Cihlar 1996; Dhakar et al., 2019; Eklundh et al., 2001; Fang and Liang 2003; Ganguly et al., 2012; Wang et al., 2019), there are no public Landsat LAI products available for use thus far; furthermore, most algorithms have been proposed under specific conditions, which cannot guarantee their global applicability. In this article, the LAI was estimated from the Landsat NDVI. First, according to the method proposed by Jacquemoud (1993), the PROSPECT+4SAIL model was used to simulate the red and near-infrared channel SRs of Landsat 8. Then, the NDVI was calculated from the SRs, and finally, the empirical relationship between the NDVI and LAI was established.

The main input parameters of the PROSPECT +4SAIL model are biophysical parameters, soil reflectance spectra, hotspot, leaf angle and other parameters. The biophysical parameters include the leaf structure parameter (N), chlorophyll $a+b$ content (C_{ab}), carotenoid content (C_{ar}), brown pigment concentration (C_{brown}), equivalent water thickness (C_w), dry matter content (C_m), LAI, etc. Detailed settings are shown in Table 5, which are based on observations during Leaf Optical Properties

Table 3

Leaf emissivity values for different composited vegetation land cover types.

IGBP Class	Composite Type	Leaf Emissivity			Sources
		Landsat5	Landsat7	Landsat8	
1–5	Forest	0.962	0.962	0.961 (0.963)	Mean of 2, 24 and 118 leaf emissivity spectra from ASTER, MODIS and ECOSTRESS spectral library
6,7	Shrubland	0.959	0.959	0.958 (0.960)	Mean of 20 leaf emissivity spectra from ECOSTRESS spectral library
8,9	Savanna	0.969	0.968	0.967 (0.970)	50% forest + 50% grassland
10	Grassland	0.976	0.974	0.973 (0.978)	Mean of 1 and 4 grass emissivity spectra from ASTER and ECOSTRESS spectral library
12,14	Cropland	0.960	0.961	0.966 (0.959)	Mean of 4 and 39 emissivity spectra measured by (Li et al., 2014) and (Ma and Xiao 2017)
11,16,254	Other	0.965	0.965	0.965 (0.966)	Mean value of above five types

Table 4

Soil background emissivity values for different composited vegetation land cover types.

IGBP Class	Composite Type	Soil background Emissivity			Sources
		Landsat5	Landsat7	Landsat8	
1–5	Forest	0.975	0.968	0.964 (0.967)	Mean of samples of Alfisols in AST_05
6,7	Shrubland	0.966	0.964	0.964 (0.969)	Mean of samples of Aridisols in AST_05
8,9	Savanna	0.966	0.964	0.964 (0.969)	Mean of samples of Aridisols in AST_05
10	Grassland	0.966	0.964	0.964 (0.969)	Mean of samples of Aridisols in AST_05
12,14	Cropland	0.977	0.973	0.971 (0.971)	Mean of samples of Mollisols in AST_05
11,16,254	Other	0.973	0.968	0.965 (0.969)	Mean value of above three soil types

EXperiment 93 (LOPEX93) (Hosgood et al., 1994). A total of 17 soil reflectance spectra belonging to four soil types, alfisols, aridisols, mollisols, and spodosols, were entered into the model. The parameters shown in Table 5 were randomly sampled 1200 times within this range, and finally, a total of 20,400 canopy reflectance data points were generated. According to the simulated canopy reflectance and input LAI data, the coefficients of the empirical relationship between LAI and NDVI were determined.

(3) Landsat LSE was calculated. Given the soil type and vegetation types, we can determine the leaf emissivity and soil background emissivity. The LAI was estimated through the established empirical relationship with the NDVI input. After the three inputs were determined, LSE was interpolated from the LUT.

3.1.3. Snow/ice and water surfaces

Based on the field-measured and model-simulated emissivity, the LSEs of water and snow/ice in the nadir observation changed very little (Cheng et al. 2010, 2019; Hori et al., 2006; Wu and Smith 1997); therefore, the LSEs were set to fixed values. The LSEs of water and snow/ice were calculated according to the ASTER/MODIS spectral library data and the spectral response function of the Landsat 5/7/8 TIR channel. According to the Landsat Level-2 pixel quality band, the LSEs of water and snow/ice were set to 0.987 and 0.977 for Landsat 5 channel 6, 0.997, and 0.982 for Landsat 7 channel 6, and 0.991 (0.986) and 0.990 (0.975) for Landsat 8 channel 10 (11).

3.2. Atmospheric correction

According to radiative transfer theory, the radiance measured by using the thermal infrared channel at the TOA consists of three parts: the radiance emitted directly by the surface, upward atmospheric thermal radiance, and downward atmospheric thermal radiance reflected by the surface (Li et al., 2013a). Thus, atmospheric effects must be corrected before the recovery of LST. The MERRA2 reanalysis product was used to implement atmospheric correction in this article, considering its long observation period and good data quality. The process of generating the needed atmospheric variables from MERRA 2 is shown in Fig. 5. Before this, we needed to determine the atmospheric variables required by RTTOV. Variables such as pressure levels, temperatures on levels, water

Table 5
The boundary ranges of the main input parameters of the model.

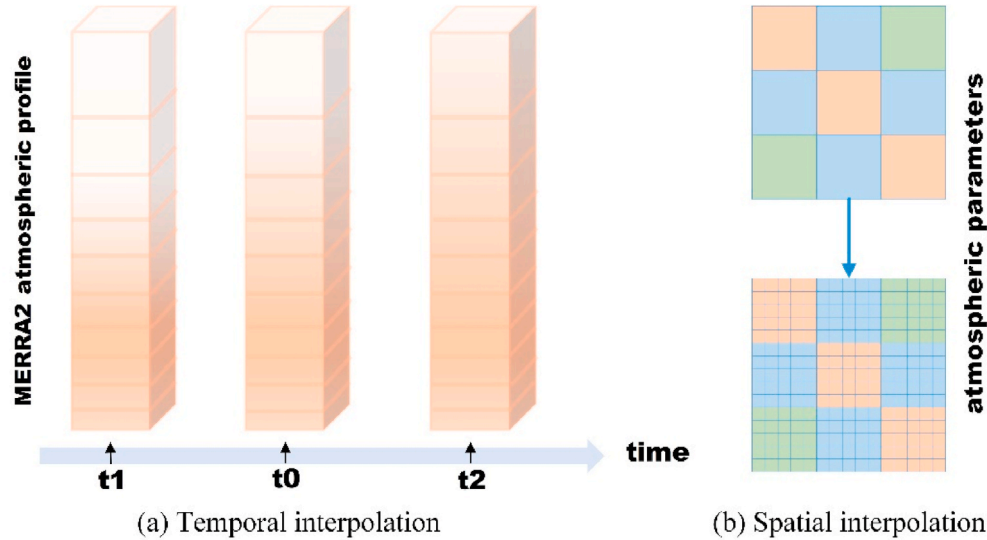| parameter	N	C_{ab}	C_{ar}	C_{brown}	C_w	C_m	LAI	hotspot	leaf_angle
min	1.0	0	0	0	6.3e-05	0.0019	0	0.01	30
max	3.0	100	40	1	0.04	0.0165	6	0.1	80

Fig. 5. Schematic diagram for temporal interpolation and spatial interpolation of atmospheric variables; t0 is the Landsat overpass time, and t1 and t2 are the MERRA2 UTC time before and after Landsat overpass time, respectively.

vapor on levels, surface pressure, 2 m temperature, surface skin temperature, latitude, longitude, and satellite zenith angle are mandatory for RTTOV. Note that the surface pressure determines the surface location within the vertical profile in RTTOV rather than the elevation, and the elevation interpolation described in the studies of (Rosas et al., 2017; Yang et al., 2020) is not needed here.

Then, we temporally interpolated the atmospheric variables to the Landsat overpass time. Since the MERRA2 reanalysis product is available at 6-h time steps, the atmospheric variables before and after the Landsat overpass time were linearly interpolated to match the Landsat overpass time. The interpolated atmospheric variables were then entered into RTTOV to compute three atmospheric parameters at each MERRA2 pixel. As it is computationally intensive to run RTTOV for all Landsat pixels, we spatially interpolated the three atmospheric
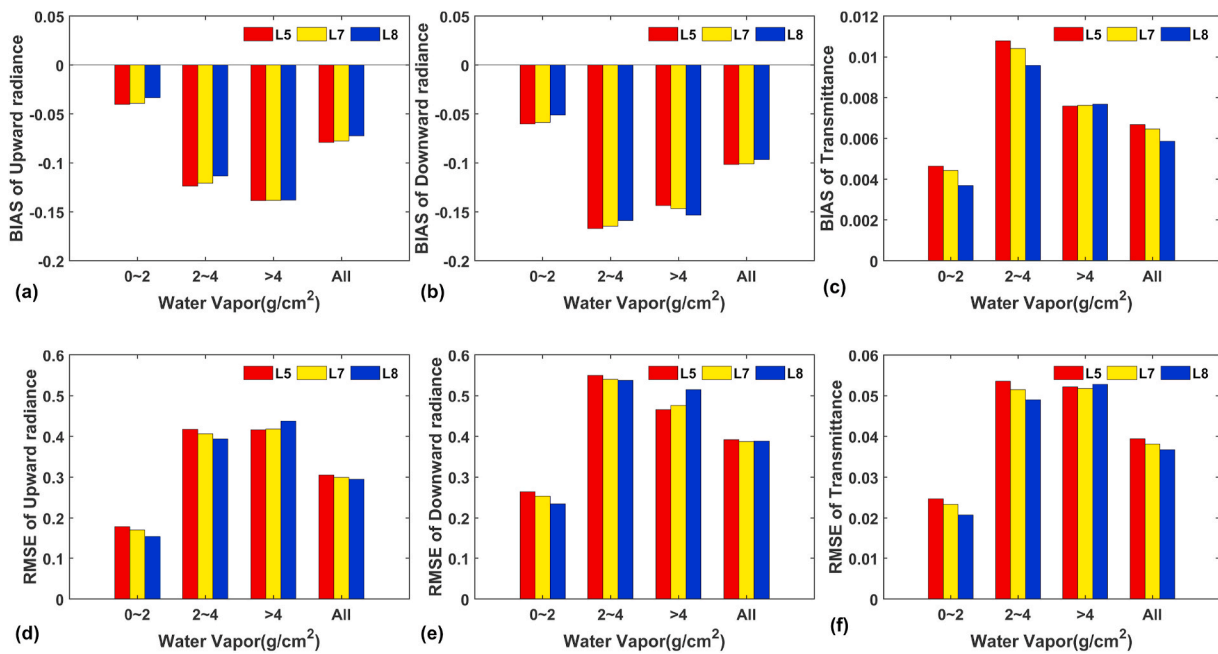

Fig. 6. Histograms of the biases (a-c) and RMSEs (d-f) between the atmospheric upward radiance, downward radiance, and transmittance simulated from MERRA-2 reanalysis product and that simulated from WYO observations. The units of the atmospheric upward (downward) radiance and transmittance are $W/(m^2 \cdot \mu m \cdot sr)$ and unitless, respectively.

parameters at each MERRA2 pixel to each Landsat pixel using the nearest-neighbor interpolation method.

4. Results and analysis

4.1. The accuracy of atmospheric correction

To investigate the performance of MERRA 2 atmospheric variables in the atmospheric correction, the atmospheric parameters ($L_i^\uparrow$, $L_i^\downarrow$ and τ_i) calculated from the radiosounding profiles using MODTRAN5 code were used to validate the atmospheric parameters calculated from the MERRA2 reanalysis product. The radiosounding profiles in January, April, July, and October 2013 were collected from 163 global radiosonde stations, and detailed information about the radiosonde stations please refer to our previous research (Meng and Cheng 2018). According to the range of water vapor content, we divided the atmospheric parameters into four groups: 0–2 g/cm², 2–4 g/cm², >4 g/cm², and all ranges to evaluate the accuracy of atmospheric correction. The distributions of biases and RMSEs for the atmospheric upward radiance, downward radiance, and transmittance are shown in Fig. 6.

When the water vapor content was between 0 and 4 g/cm², the uncertainty of three atmospheric parameters for Landsat 5 was the largest and followed by Landsat 7 and Landsat 8. The biases (RMSEs) of atmospheric upward radiance were between −0.033 (0.154) and −0.124 (0.418) $W/(m^2 \cdot \mu m \cdot sr)$ for Landsat 5/7/8, whereas those values were between −0.051 (0.234) and −0.167 (0.549) $W/(m^2 \cdot \mu m \cdot sr)$ for atmospheric downward radiance. The biases (RMSEs) of atmospheric transmittance were between 0.004 (0.021) and 0.011 (0.054) for Landsat 5/7/8.

When the water vapor content was larger than 4 g/cm², the biases of atmospheric upward radiance for Landsat 5/7/8 were similar (about −0.138 $W/(m^2 \cdot \mu m \cdot sr)$), but the RMSEs of atmospheric downward radiance for Landsat 8 was larger than those of Landsat 7 and Landsat 5. The biases (RMSEs) of atmospheric downward radiance for Landsat 8 was the largest followed by Landsat 7 and Landsat 5, and the biases (RMSEs) were between −0.144 (0.466) and −0.154 (0.514) $W/(m^2 \cdot \mu m \cdot sr)$. The biases (RMSEs) of atmospheric transmittance for Landsat 5/7/8 were similar, with biases (RMSEs) was about 0.008 (0.052).

The overall biases (RMSEs) were between −0.079 (0.305) and −0.072 (0.295), −0.102 (0.392) and −0.097 (0.387) $W/(m^2 \cdot \mu m \cdot sr)$ for the atmospheric upward and downward radiance of Landsat 5/7/8, respectively. The overall biases (RMSEs) were between 0.007 (0.039) and 0.006 (0.037) for the atmospheric transmittance of Landsat 5/7/8.

In this section, simulation data were used to evaluate the impact of the atmospheric parameters on the accuracy of LST retrieval. First, the atmospheric parameters calculated from the radiosonde profiles were used to simulate the TOA radiances. Then, LSTs were retrieved with the RTE method using the atmospheric parameters calculated from the MERRA2 reanalysis product. Finally, the retrieved LSTs were compared with the initial LSTs. In the simulation, the initial LSTs were set as T0-5, T0, T0+5, T0+10 and T0 + 20 K (T0 is the bottom layer temperature of the radiosonde profile), which have been used in other studies (Jiménez-Muñoz et al., 2014). The land surface emissivity varied from 0.89 to 0.99 with a step of 0.01.

Fig. 7 shows the evaluation results for the retrieved LST. The overall biases (RMSEs) of the LST were 0.554 (1.940), 0.505 (1.749), and 0.418 (1.467) K for Landsat 5, Landsat 7, and Landsat 8, respectively. The Landsat 5 LST had the highest biases (RMSEs) under various water vapor content groups, followed by Landsat 7 LST and Landsat 8 LST. The biases (RMSEs) of the Landsat 5/7/8 LST increased with the increase of water vapor content under different water vapor content groups. The biases (RMSEs) of LST ranged from 0.157 (0.481) to 1.688 (3.932) K for Landsat 5, 0.149 (0.446) to 1.508 (3.527) K for Landsat 7, 0.122 (0.380) to 1.242 (2.949) K for Landsat 8.

As shown in Fig. 7, the impacts of the atmospheric parameters on the accuracy of the LST gradually increased with water vapor content. When water vapor was less than 4 g/cm², the atmospheric parameters had little impact on the accuracy of LST. When the water vapor content was larger than 4 g/cm², the atmospheric parameters had a greater influence on the accuracy of LST. The larger atmospheric correction errors may have been improved by developing atmospheric profiles with higher temporal and spatial resolutions.

4.2. Validation of the estimated LSE

4.2.1. Nonvegetated surfaces

A total of tens of millions of samples were obtained for ten types of soil (i.e., Alfisols, Aridisols, Entisols, Gelisols, Inceptisols, Mollisols, Oxisol, Ultisols, Vertisols, and sand). In this article, 80% of the samples were used as the training dataset to fit the relationship between Landsat LSE and Landsat SRs, and 20% of the data were used as the test dataset. The fitted coefficients of Equation (5) are shown in Table 6. According to the evaluation results using the test data, RMSEs were 0.0042, 0.0044, 0.0055, and 0.0046 for Landsat 5/b6, Landsat 7/b6, Landsat 8/b10 and Landsat 8/b11, respectively. The mean absolute errors (MAEs) were 0.0029, 0.0034, 0.0043 and 0.0035.

The in situ data are important for validating the performance of the new method. Although there are no synchronous in situ LSE data, the in situ data in Table 1 collected from different researchers were used to conduct a preliminary validation of the new method. Due to the different measurement times, the Landsat images used at different sites were also different, and detailed information can be found in Table 7. The LSE was calculated using Equation (5) with coefficients provided in Table 6. The validation results are shown in Fig. 8.

The absolute average bias of Landsat 5/7/8 LSE obtained by the new algorithm was generally within 0.01, and the standard deviations were all less than 0.002. The average bias of Landsat 5 LSE at Kelso,
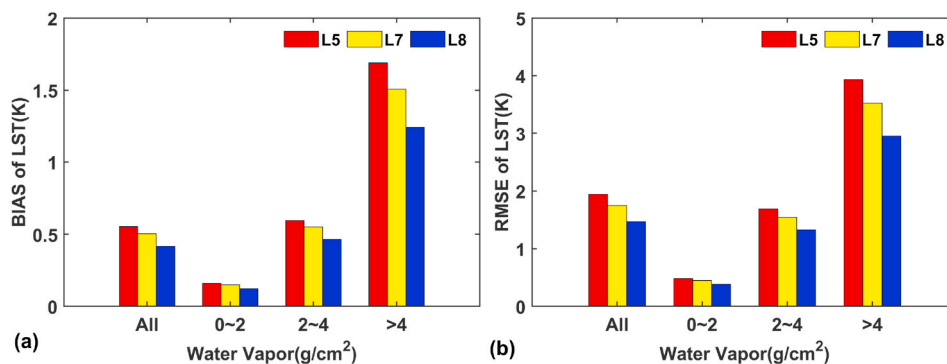

Fig. 7. Histograms of the biases (a) and RMSEs (b) between the retrieved LST that used MERRA-2 reanalysis product and the referenced LST with various water vapors.

Table 6
The fitted coefficients of Equation (5) for Landsat 5/7/8.

	a_0	a_1	a_2	a_3	a_4	a_5	a_6	a_7
L5/b6	0.9644	−0.0567	0.1043	−0.0481	0.0082	−0.0065	–	0.0040
L7/b6	0.9648	−0.0660	0.0695	−0.0485	0.0450	0.0301	–	−0.0544
L8/b10	0.9607	0.084	−0.0358	−0.0147	−0.1008	0.1010	0.0277	−0.0537
L8/b11	0.9642	0.0064	−0.1504	0.1285	0.0133	−0.0031	−0.0137	0.0082

Table 7
The time periods of Landsat 5/7/8 images used for LSE validation.

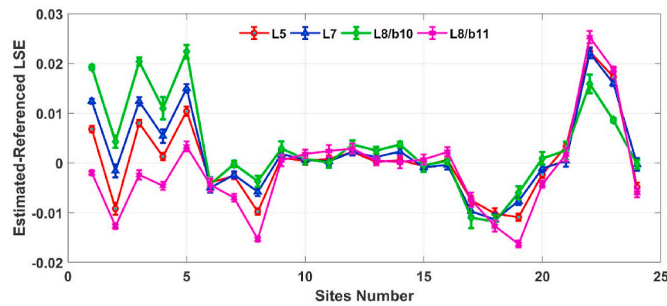| Satellite	Period
Landsat5	2006–2010
Landsat7	2006–2010(sites1~8,24), 2013–2017(sites 9–14), 2010–2014 (sites15~16), 2011–2015(sites17~20), 2013–2017(site21), 2009–2013 (sites22~23)
Landsat8	2014–2018

Fig. 8. The mean biases between retrieved Landsat land surface emissivity (LSE) and referenced LSEs at 24 sites. The error bars denote the standard deviation of retrieved Landsat LSE.

HuaZhaiZi, and Shenshawo1 was approximately 0.01. The average biases of Landsat 5 LSEs at the Taklimakan1 and Taklimakan2 sites were poor, with average biases equal to 0.0224 and 0.0173, respectively. The average biases of Landsat 7 LSE at the Great Sands, Killpecker, Kelso, HuaZhaiZi, and Taklimakan2 sites were 0.0124, 0.0124, 0.015, −0.0114, and 0.016, respectively. The average bias of Landsat 7 LSE at the Taklimakan1 site was 0.0221, which was the poorest performance. For Landsat 8 channel 10, the average biases of Landsat 8 LSE at the Little Sahara, Gebi, HuaZhaiZi, and Taklimakan1 sites were 0.011, −0.011, −0.0118, and 0.0159, respectively. The average bias of Landsat 8 LSE at the Great Sands, Killpecker, and Kelso sites was poor, with average biases equal to 0.0192, 0.0204 and 0.0224, respectively. In terms of Landsat 8 channel 11, the average biases of Landsat 8 LSE at the White Sands, Moses Lake, HuaZhaiZi, and Shenshawo1 sites were −0.0127, −0.0153, −0.0127, and −0.0163, respectively. The average biases of Landsat 8 LSE at the Taklimakan1 and Taklimakan2 sites were 0.0253 and 0.0188, respectively.

The larger LSE biases at a few sites (e.g., Great Sands, Killpecker, and Kelso) can be attributed to the following two reasons: on the one hand, according to the validation results of Hulley et al. (2009), the retrieved ASTER LSEs and in situ values were very different at these sites. The referenced LSEs used in this article were obtained on the basis of ASTER LSEs; therefore, this phenomenon is taken for granted. On the other hand, the samples were collected from the field and transferred to the laboratory to measure their emissivity spectra. Field sampling disturbs the surface microstructure, which may cause measurement errors in emissivity spectra (Cheng et al., 2014a). From the above validation results, we can conclude that the new LSE estimation algorithm can obtain an accurate LSE over nonvegetated surfaces and provide a more reliable input parameter for LST retrieval.

4.2.2. Vegetated surfaces

Due to the lack of ground measurements available for validating the performance of the new algorithm over vegetated surfaces, the theoretical uncertainty of LSE estimated by the LUT method is provided here. Assuming the deviation of assigned leaf emissivity and soil background emissivity for each land cover type is negligible, the uncertainty of LSE over vegetated surfaces mainly comes from the uncertainty of the retrieved LAI.

To evaluate the influence of the LAI on the LSE estimation, the uncertainty of LSE was estimated by comparing the difference of LSE before and after the random noise added to the LAI. The specific process is as follows:

(1) Assuming that the range of the LAI is between 0 and 6, sixty-one LAIs were generated with a step of 0.1, which were recorded as LAI_i ($i = 1, 2, 3 … 61$).

(2) One thousand random noises with a Gaussian distribution of $N(0, σ^2)$ were added to each LAI_i, and $σ$ was set as follows by referring to the studies of Jin et al. (2019).

$$σ = \begin{cases} 0.5, & 0 \leq LAI_i \leq 2 \\ 0.8, & 2 < LAI_i \leq 6 \end{cases} \qquad (9)$$

(3) The LSEs before and after the random noise was added to the LAI were recorded as $ε^{before}$ and $ε^{after}$. Among them, the settings of leaf emissivity and soil background emissivity are shown in Tables 3 and 4, respectively.

(4) The variation in MAE between $ε^{before}$ and $ε^{after}$ under different vegetation land cover types is shown in Fig. 9.

$$MAE = \frac{\sum_{i=1}^{n} \left| ε_i^{after} - ε_i^{before} \right|}{n} \qquad (10)$$

In the case of LAI∈[0,2], for Landsat 5 channel 6, the average MAE of LSE on grassland was 0.0034, which is larger than that on savanna, shrubland, others, forest, and cropland, in which those values were between 0.0029 and 0.0005, respectively. For Landsat 7 channel 6, the average MAE of LSE on grassland was 0.0036, whereas those values were between 0.0031 and 0.0009 for other land cover types. The average MAE of LSE on grassland was 0.0035 and 0.0031 for Landsat 8 channel 10 and channel 11, respectively, whereas those values were all less than 0.0030 and 0.0025, respectively, on the other vegetated surfaces. In the case of LAI ∈ (2,6), the average MAEs of Landsat 5/7/8 LSE were all less than 0.0002 on grassland, savanna, shrubland, others, forest, and cropland. The simulation results show that the average MAE of Landsat 5/7/8 LSE caused by LAI uncertainty was less than 0.004, whether in the case of LAI∈[0,2] or LAI∈(2,6). As shown in Fig. 9, when the LAI was less than 1.0, the maximum uncertainty of LSE on vegetated surfaces caused by the uncertainty of the LAI could reach 0.01, which indicates that due to the uncertainty of the LAI, the Landsat LSE retrieved from our method may have larger uncertainty on sparse vegetated surfaces. As the LAI increases, the error in LSE caused by the LAI could be negligible, which shows that the uncertainty of the estimated LAI had little impact on the Landsat LSE estimated on dense vegetated surfaces.
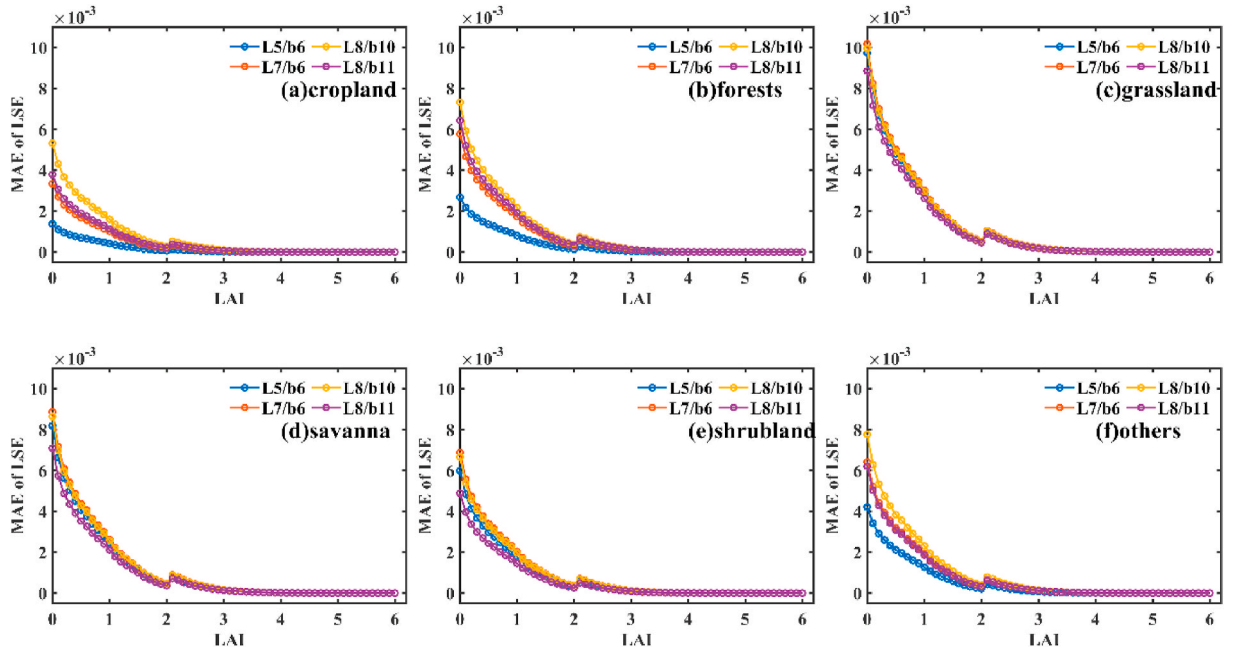
Fig. 9. MAEs of Landsat 5/7/8 land surface emissivity (LSE) on different vegetation land cover types due to errors in the leaf area index (LAI). Land cover type is cropland (a), forests (b), grassland (c), savanna (d), shrubland (e), and others (f).

4.3. Uncertainty of derived LSTs

4.3.1. Sensitivity analysis

The RTE algorithm developed in this study requires five input parameters, including the at-sensor brightness temperature, LSE and three atmospheric parameters ($L_i^\uparrow$, $L_i^\downarrow$ and τ_i). To analyze the effects of the input parameters on the retrieved LST, the following formula was used

to estimate the uncertainty of LSTs (Qin et al., 2001).

$$\delta T_s = |T_s(x + \delta x) - T_s(x)| \tag{11}$$

where δT_s is the error of the retrieved LST, x is the input parameters, δx is the possible error of the input parameters, and $T_s(x+\delta x)$ and $T_s(x)$ are the LST calculated using Equation (4) for $x + \delta x$ and x, respectively.
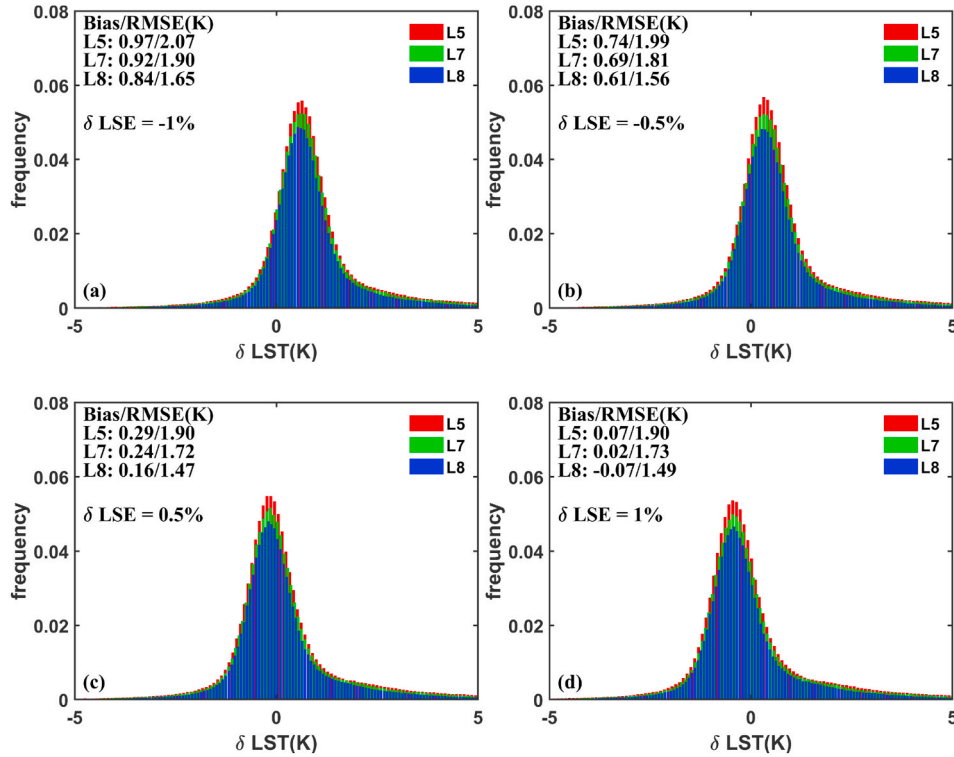

Fig. 10. Sensitivity analysis of the RTE algorithm. δLSE represents error in land surface emissivity (LSE) and the LSE was set as 0.97; δT_s represents error in land surface temperature (LST) attributed to the errors of at-sensor brightness temperature, atmospheric parameters, and LSE. Errors in LST when δLSE equal to -1% (a); δLSE equal to -0.5% (b), δLSE equal to 0.5% (c), δLSE equal to 1% (d).

Sensitivity analysis was performed using simulated data under several conditions. The total error of LST was attributed to the error of at-sensor brightness temperature, LSE, and atmospheric parameters. In this simulation, 100 random noise with a Gaussian distribution of $N(0, 0.4^2)$ was added to each at-sensor brightness temperature. The LSE was set to 0.97, and the LSE error ranged from −1% to 1% with a step of 0.5%. For convenience, the uncertainty of the atmospheric parameters was simulated using 2000 atmospheric profiles, which were randomly selected from radiosounding profiles and the MERRA-2 reanalysis product. The total error of the retrieved LST is shown in Fig. 10.

When the LSE error was equal to −1%, the bias (RMSE) of the total error for Landsat 5, Landsat 7 and Landsat 8 LST was 0.97 (2.07), 0.92 (1.90), and 0.84 K (1.65 K), respectively, whereas those values were 0.74 (1.99), 0.69 (1.81), and 0.61 K (1.56 K), respectively, for the LSE error equal to −0.5%. When the LSE error was equal to 0.5% (1%), the biases of the total error for Landsat 5 LST, Landsat 7 and Landsat 8 LST were 0.29 (0.07), 0.24 (0.02), and 0.16 K (−0.07 K), respectively, whereas the RMSE of δT_s was 1.90 (1.90), 1.72 (1.73), and 1.47 K (1.49 K), respectively.

4.3.2. Validation of the retrieved LSTs

There were three Landsat collection tiers for each satellite, and only Tier 1 Landsat scenes were used for calculating LST. Before LST validation, invalid pixels affected by clouds and cloud shadows were removed according to the Landsat level-2 pixel quality channel, and only clear or snow pixels were selected for validation. In situ measurements at the SURFRAD, BSRN and Huailai sites were used to validate the retrieved Landsat LST. Moreover, the outliers were removed based on the "3σ-Hampel identifier" (Göttsche et al., 2013). Fig. 11 shows the scatterplots between Landsat LST and in situ LST for the twelve sites, and
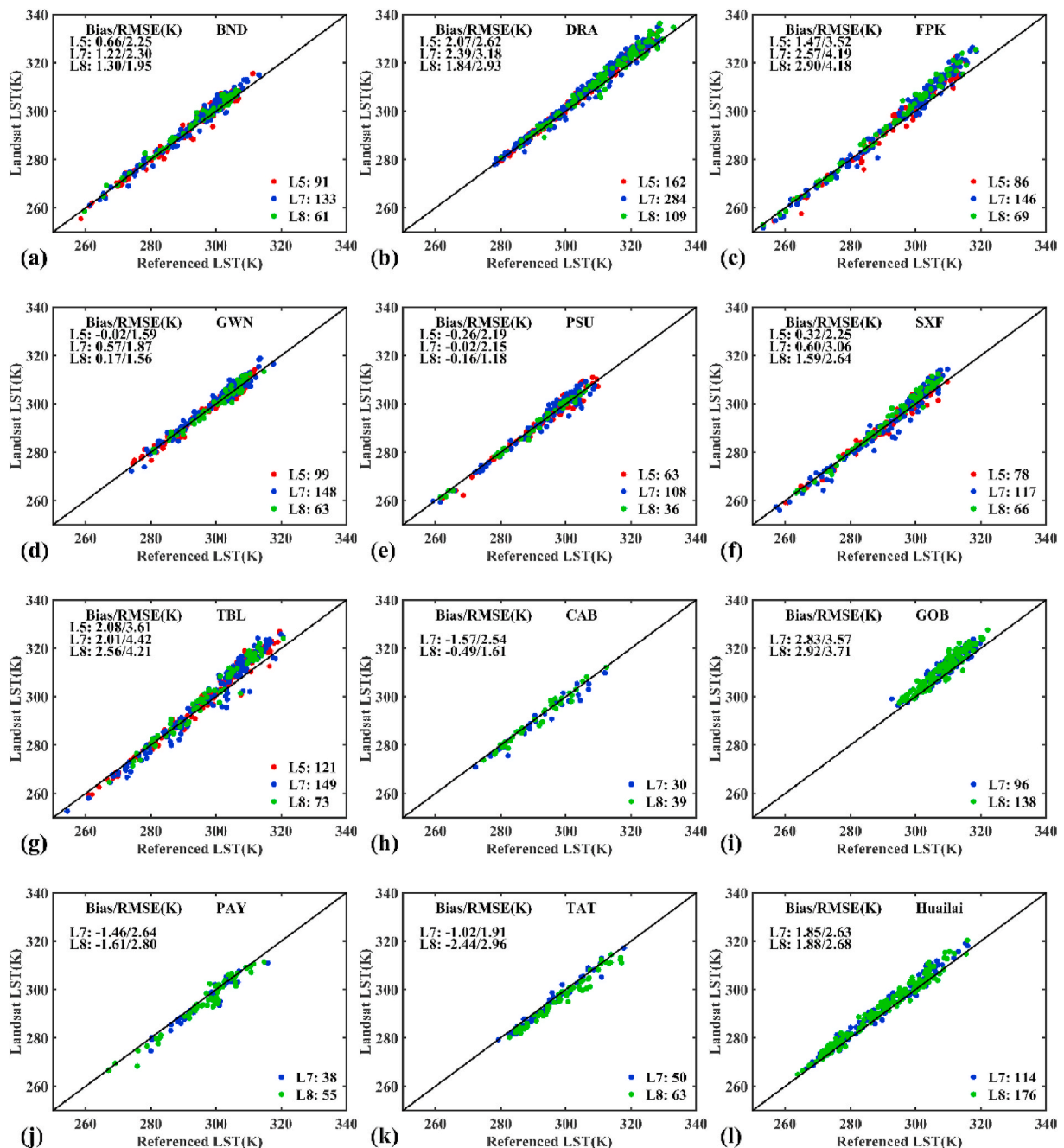

Fig. 11. Scatterplots of the retrieved Landsat land surface temperatures (LSTs) versus in situ LSTs at fourteen sites. (a-g) SURFRAD sites; (h-l) BSRN sites.

the overall validation results are shown in Table 8.

For the SURFRAD sites, the performance of the retrieved Landsat 5 LST at the BND, GWN, PSU, and SXF sites was better than that of DRA, FPK, and TBL sites, with biases and RMSEs less than 0.7 K and 2.3 K, respectively. In terms of the retrieved Landsat 7 LST, the biases and RMSEs at the GWN, PSU, and SXF sites were less than 0.6 K and 3.1 K, respectively, followed by the BND, DRA, FPK, and TBL sites. The retrieved Landsat 8 LSTs performed best at the GWN and PSU sites, followed by BND, DRA, and SXF sites, and had the worst performance at FPK, and TBL sites.

For the BSRN and Huailai sites, the retrieved Landsat 7/8 LST values were lower than in situ measurements at the CAB, PAY, and TAT sites, and the average biases were between −1.57 K (−2.44 K) and −1.02 K (−0.49 K) for Landsat 7 (Landsat 8) LST. The biases (RMSEs) of the Landsat 7/8 LST at the GOB and Huailai sites were all larger than 2.83 K (3.57 K) and 1.85 K (2.63 K), respectively.

In summary, the overall biases (RMSEs) of Landsat 5/7/8 LST estimated from our method at the SURFRAD sites were all less than 1.63 K (3.21 K). The overall biases at the BSRN and Huailai sites were all equal to 1.00 K for Landsat 7 and Landsat 8 LST, whereas the overall RMSEs were 2.84 K and 3.00 K, respectively. The performances at the DRA, FPK, and TBL sites were worse than those at the BND, GWN, PSU, and SXF sites. This phenomenon can be explained by the following reason: as discussed in Malakar et al. (2018), the spatial heterogeneity in cover types around the DRA, FPK, and TBL sites was stronger than that at the other four sites, which was not suitable for the validation of LST products with 100 m or higher resolution. When the high spatial heterogeneity sites DRA, FPK, and TBL sites were excluded, the overall biases (RMSEs) of Landsat 5, 7, and 8 LST were equal to 0.20 K (2.06 K) and 0.62 K (2.36 K), and 0.84 K (1.99 K), respectively. The above validation results demonstrate that the operational method can be used for estimating LST from Landsat series TIR data.

5. Discussion

5.1. Comparison with previous LSE studies

For nonvegetated surfaces, there are three methods to calculate LSE, i.e., the NDVI-based emissivity threshold method (NDVI^{THM}) (Sobrino and Raissouni 2000), simplified NDVI^{THM} (SNDVI^{THM}) (Sobrino et al., 2010), and improved NDVI^{THM} (INDVI^{THM}) (Tang et al., 2015). In this article, the retrieved Landsat LSE was compared with the Landsat LSE estimated from NDVI^{THM} and INDVI^{THM}. Detailed information about the algorithm coefficients can be found in Table 9, and the validation results for different algorithms are shown in Fig. 12. The SNDVI^{THM} is not considered here because the variability of emissivity values for soils is greater than that for vegetation ones (Sobrino et al., 2004); therefore, it is difficult to select typical emissivity values for bare soil. Although some researchers have also used these methods to estimate Landsat LSE (Chatterjee et al., 2017; Ren et al., 2017; Windahl and Beurs 2016; Zhou et al., 2011), the coefficients were not provided in their articles; therefore, it is difficult to compare.

Among most of all the 24 sites, the accuracy of the Landsat 5/7 LSEs estimated from our method was better than that of the LSEs estimated from NDVI^{THM}. The average biases of Landsat 5 LSE at all sites were 0.0006 and 0.0026 for our method and NDVI^{THM}, respectively, whereas those values were 0.0019 and 0.0076, respectively for Landsat 7 LSE. At

Table 8
Statistics for the validation of the Landsat 5/7/8 LST.

Site	Bias/RMSE (K)		
	Landsat 5	Landsat 7	Landsat 8
All	1.11/2.72	1.41/3.13	1.32/3.01
SURFRAD	1.11/2.72	1.54/3.21	1.63/3.02
BSRN	–	0.55/2.95	0.48/3.18

Table 9
Equations for the NDVI^{THM} and INDVI^{THM} applied to different sensors.

Satellite	Equation	Source
Landsat 5	$\varepsilon_6 = 0.979 - 0.035\rho_3$	ASTER spectral library (Sobrino et al., 2008)
Landsat 7	$\varepsilon_6 = 0.9796 - 0.0408\rho_3$	ASTER spectral library (Kodimalar et al., 2020)
Landsat 8	$\varepsilon_{10} = 0.979 - 0.046\rho_4$ $\varepsilon_{11} = 0.982 - 0.027\rho_4$	ECOSTRESS spectral library (Vanhellemont 2020)
Landsat 8	$\varepsilon_{10} = 0.973 - 0.047\rho_4$ $\varepsilon_{11} = 0.984 - 0.026\rho_4$	MODIS spectral library (Yu et al., 2014)
Landsat 8	$\varepsilon_{10} = 0.9689 + 0.0182\rho_1 - 0.2344\rho_2 + 0.5513\rho_3 - 0.4303\rho_4 + 0.2811\rho_5 - 0.4352\rho_6 + 0.3022\rho_7$ $\varepsilon_{11} = 0.9780 + 0.0746\rho_1 - 0.6125\rho_2 + 0.9827\rho_3 - 0.3298\rho_4 - 0.0593\rho_5 - 0.2922\rho_6 + 0.2506\rho_7$	ASTER spectral library (Emami et al., 2016)
Landsat 8	$\varepsilon_{10} = 0.980 - 0.140\rho_2 + 0.170\rho_3 - 0.036\rho_4 - 0.083\rho_5 + 0.158\rho_6 - 0.149\rho_7$ $\varepsilon_{11} = 0.979 + 0.026\rho_2 - 0.071\rho_3 + 0.048\rho_4 - 0.056\rho_5 + 0.128\rho_6 - 0.105\rho_7$	ASTER spectral library (Li and Jiang 2018)

those sites in which our method had low accuracy, the performance of NDVI^{THM} was worse than that of our method. At the Moses Lake, Gebi, HuaZhaiZi and Shenshawo1 sites, the accuracy of Landsat 5 LSE estimated from NDVI^{THM} was better than that of our method. At the Gebi, HuaZhaiZi and Shenshawo1 sites, the accuracy of Landsat 7 LSE estimated from NDVI^{THM} was better than that of our method.

As far as Landsat 8 is concerned, among most of all the 24 sites, the accuracy of LSE estimated from our method was better than the LSE estimated from NDVI^{THM} or INDVI^{THM} using the coefficients in other researchers' articles. Among most of all the 24 sites, the average biases of LSE estimated from our method, NDVI^{THM} and INDVI^{THM} were within 0.01. The average biases of Landsat 8 LSE (channel 10) at all sites were 0.0034, 0.0109, 0.0113, 0.0046, and 0.0124 for our method, Vanhellemont's, Emami et al.'s, Li and Jiang's, and Yu et al.'s results, whereas those values were −0.0015, 0.0023, 0.0023, 0.0046, and 0.0026, respectively for Landsat 8 LSE (channel 11).

Obviously, the estimated Landsat LSE using the NDVI^{THM} and INDVI^{THM} is larger than that estimated from our method among most of all the 24 sites. At those sites in which our method had low accuracy, the performance of NDVI^{THM} and INDVI^{THM} was like or worse than our method. The performance of NDVI^{THM} and INDVI^{THM} can be attributed to the following reason: the coefficients in NDVI^{THM} and INDVI^{THM} were obtained by using the limited soil sample spectra from the spectral library. On the one hand, the retrieved LSE was consistent with the ground measurement in some soil types; on the other hand, there may be large errors in some soil types that were not included in the samples. The above validation results show that the accuracy of Landsat LSE estimated by our method at different sites was relatively stable, and the performance on different TIR sensors was uniform.

5.2. Comparison with USGS LST product

To analyze the performance of the retrieved LSTs, we downloaded the USGS LST product of the SURFRAD sites for comparison. Landsat 5 LST products from 2001 to 2011, Landsat 7 LST products from 2011 to 2019, and Landsat 8 LST products from 2013 to 2020 were downloaded. The outliers of the retrieved LSTs and USGS LSTs were removed based on the "3σ-Hampel identifier". The bias, STD, and RMSE of the retrieved LST and USGS LST at the SURFRAD sites are shown in Fig. 13.

The validation results with in situ measurements at the SURFRAD sites show that the bias of the retrieved Landsat 5 LST was lower than that of the USGS LST, while the bias of the retrieved Landsat 7 and
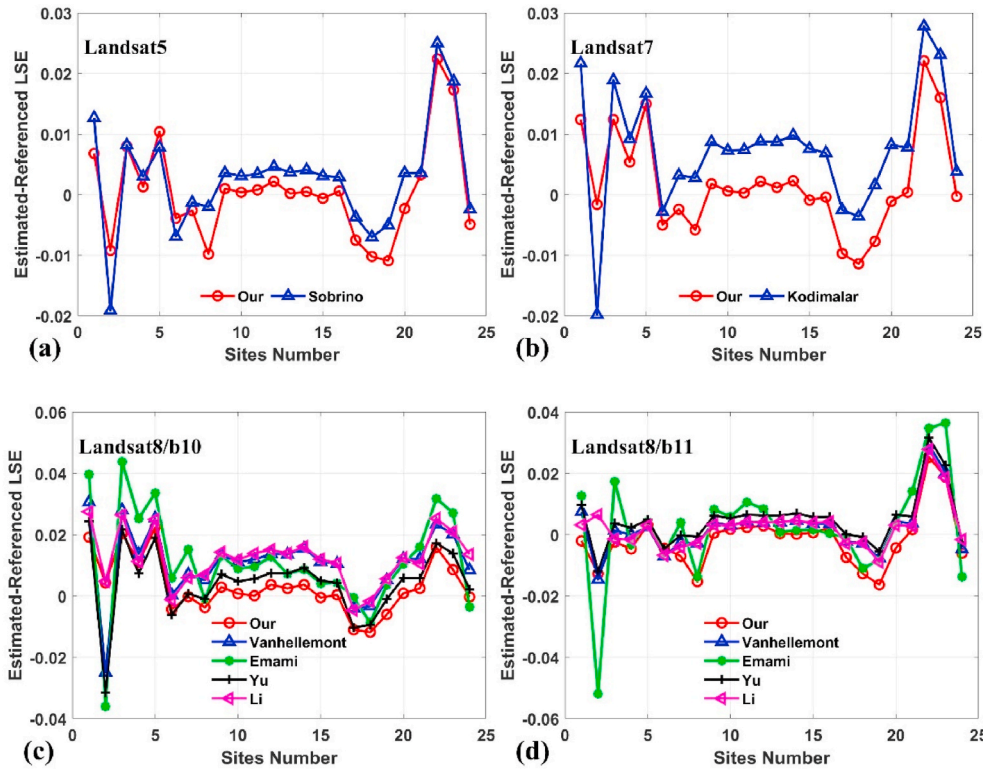
Fig. 12. The average biases between retrieved Landsat land surface emissivity (LSE) using different methods and referenced LSEs at 24 sites. Validation result of Landsat 5 LSE (a), Landsat 7 LSE (b), and Landsat 8 LSE (c-d).
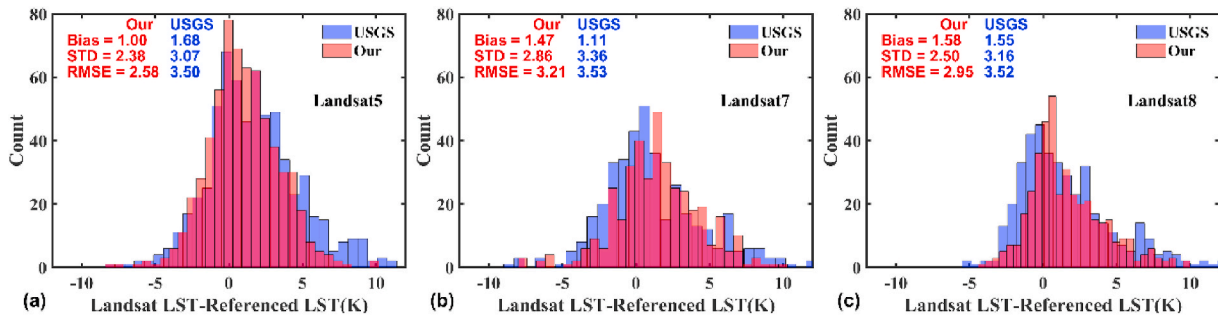

Fig. 13. Histograms of Landsat land surface temperature (LST) versus in situ LST at the SURFRAD sites. Validation result of Landsat 5 LST (a), Landsat 7 LST (b), and Landsat 8 LST (c).

Landsat 8 LST was slightly higher than that of the USGS LST. The biases between the retrieved (USGS) Landsat 5/7/8 LST and in situ LST were less than 1.58 K (1.68 K). The STD and RMSE of the retrieved Landsat 5/7/8 LST were all less than those of the USGS LST. The RMSEs between the retrieved (USGS) Landsat 5/7/8 LST and in situ LST were less than 3.21 K (3.53 K). These validation results indicate that the Landsat 5/7/8 LST retrieved using our method can achieve better accuracy than the USGS LST product.

In addition, we found large LST differences exist between the retrieved LST and USGS LST at the BND, SXF, and TBL sites. To further analyze whether large LST differences of those sites were caused by LSE differences, the time series of the NDVI and LSE are shown in Fig. 14. As shown in Fig. 14, there are some discontinuities in the curve, where the land surface was covered with snow. Because some Landsat sensor channels were saturated during data capture, the NDVI values were set to null, but the LSEs were calculated according to the pixel quality assessment values if the pixels were water or snow.

As shown in Fig. 14, except for snow pixels, the USGS LSEs at the BND and TBL sites were invariant with the change in NDVIs, whereas the

retrieved LSEs at these two sites could reflect the temporal changes in vegetation coverage. Compared with the retrieved LSTs, the incorrectly underestimated USGS LSEs led to overestimations of approximately 0.6, 0.5, and 0.3 K for Landsat 5, Landsat 7, and Landsat 8 LST at the BND site, respectively, and those values were 3.3, 1.7, and 2.5 K at the TBL site, respectively. Both USGS LSEs and the retrieved LSEs at the SXF site could reflect the temporal changes in vegetation coverage. Compared with the USGS LSEs, the retrieved LSEs were underestimated, especially when the NDVI values were high. This may explain the positive biases of the retrieved LST at the SXF site. The biases between the retrieved (USGS) LST and in situ LST were 0.13 (−0.41), 1.59 (0.34), and 1.39 K (0.02 K) for Landsat 5, Landsat 7, and Landsat 8 LST, respectively. However, the STDs (RMSEs) of the retrieved Landsat 5, Landsat 7, and Landsat 8 LST were all less than those of the USGS LST at the SXF site.

5.3. Comparison with previous LST studies

To further analyze the performance of the retrieved LSTs, we compared our results to those of previous studies. Malakar et al. (2018)
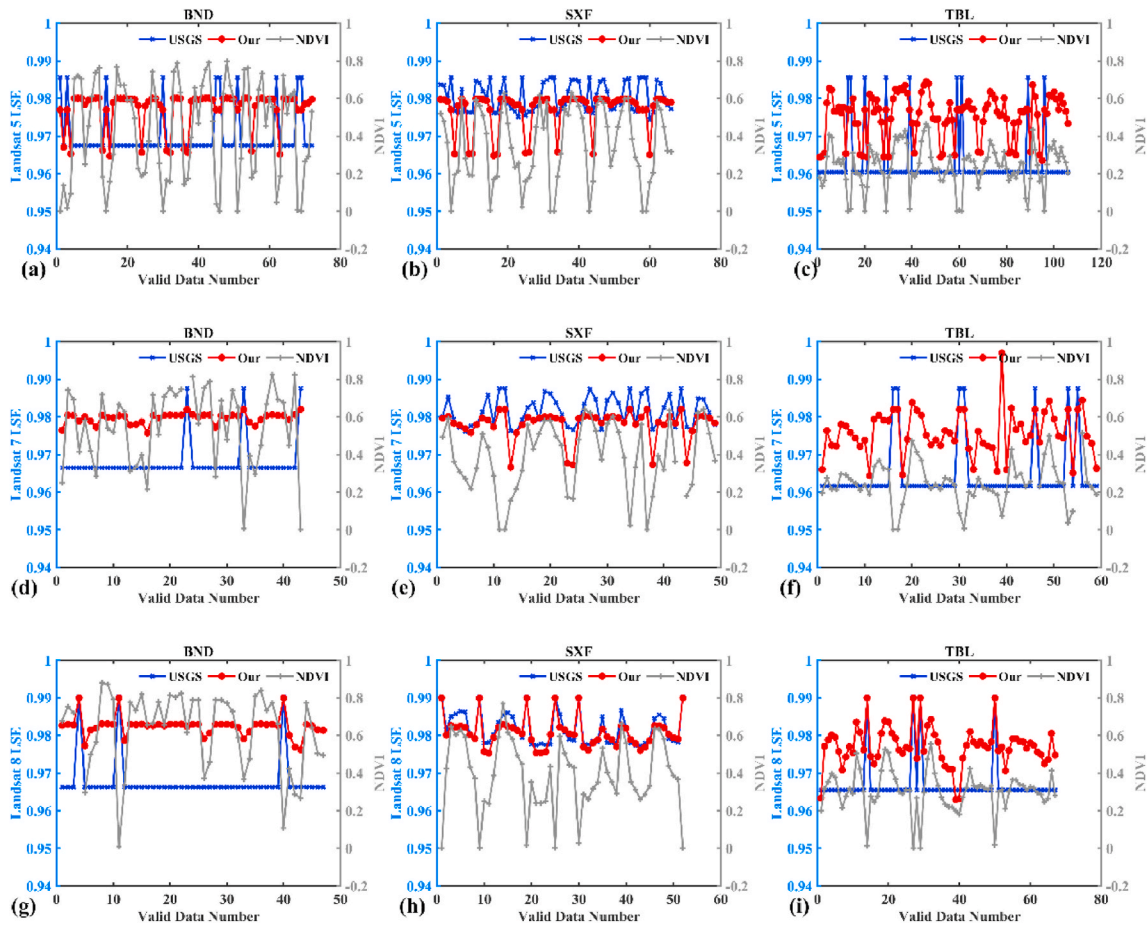
Fig. 14. Time series of NDVI and LSE at BND, SXF, and TBL sites. Graphs between NDVI and Landsat 5 LSE (a-c), Landsat 7 LSE (d-f), and Landsat 8 LSE (g-i).

estimated LST from Landsat 5/7 data using RTE algorithm and validated LST used the measurements from four SURFRAD sites. Duan et al. (2020) also investigated the accuracy of Landsat 5/7/8 LST product using in situ measurements from SURFRAD, ARM, and NDBC sites. Sekertekin and Bonafoni (2020) evaluated the performance of Landsat 5/7/8 LST retrieval methods using different LSE model, and validated LSTs with measurements from five SURFRAD sites. Moreover, the RMSEs of Landsat 8 LST estimated from RTE method ranged from 2.3 K to 2.95 K based on the validation with the limited matchup (approximately 20) (García-Santos et al., 2018; Meng et al., 2019; Yu et al., 2014). The detail information about those validation statistics for Landsat LST is shown in Table 10.

As shown in Table 10, the overall accuracy and uncertainty of our method at the same SURFRAD sites are similar to or even better than the validation results of previous work, especially when the high spatial heterogeneity sites DRA, FPK, and TBL sites were excluded, the overall RMSEs of Landsat 5, 7, and 8 LST were all less than 2.4 K. The validation results at the CAB and GOB sites were also similar to the results of Statistical Mono-Window (SMW) algorithm (Ermida et al., 2020), with biases (RMSEs) equal to −1.20 K (2.30 K) and −0.60 K (1.80 K) for Landsat 7 and Landsat 8 LST at the CAB site, respectively, whereas those values were 2.90 K (3.70 K) and 2.30 K (2.90 K) at GOB site, respectively.

The discrepancy between our validation result and that of previous work can be attributed to two reasons: (1) Rigorous quality control carried out in previous research, which can minimize the impact of cloud contamination (Duan et al., 2020; Wang et al., 2020). (2) Landsat LST product was validated with the limited matchup and the validation results may vary depending on the number of the valid matchups. Actually, although the overall accuracy of different studies is similar, it's

Table 10
Validation statistics for Landsat LST in previous studies (outside brackets) and our study (inside brackets). N is the number of valid matchups.

Satellite	Bias(K)	RMSE(K)	N	Sites	Source
Landsat 5	0.7 (0.2)	2.2 (2.1)	308 (331)	BND, GWN, PSU, SXF	Malakar et al. (2018)
Landsat 7	0.9 (0.6)	2.3 (2.4)	268 (506)		
Landsat 5	0.2–2.2 (−0.26–2.1)	2.1–3.0 (1.6–3.5)	190 (579)	BND, DRA, FPK,GWN, PSU, SXF	Duan et al. (2020)
Landsat 7	0.4–3.4 (−0.02–2.6)	1.9–4.6 (1.9–4.2)	377 (936)		
Landsat 8	0.5–3.8 (−0.16–2.9)	1.9–4.8 (1.2–4.2)	387 (404)		
Landsat 5	–	2.4 (2.4)	15 (501)	BND, DRA, FPK, GWN, PSU	Sekertekin and Bonafoni (2020)
Landsat 7	–	2.5 (2.8)	15 (819)		
Landsat 8	–	2.9–3.1 (2.7)	15 (338)		
Landsat 8	−1.0–0.1 (1.6)	2.3–3.0 (3.0)	~20 (477)	SURFRAD	García-Santos et al., (2018); Meng et al., (2019); Yu et al., (2014)

unreasonable to compare validation works under different situations, e. g. different valid matchups, different quality control methods, and LST product/ground measurements with different time periods. It is necessary to conduct comprehensive comparisons under the same conditions, and we will continue to carry out thorough validation in the next stage.

5.4. Limitation of this study

The limitations of this study can be summarized as follows: (1) The estimated LSEs on vegetated surfaces were not validated using ground measurements for the difficulty in measuring the emissivity on vegetated surfaces. We will try to collect more field measurements to validate the estimated LSEs on vegetated surfaces in the next stage. (2) At this stage, we focus on the direct validation of the estimated LSE. The impact of the LSE estimated by using different models on the accuracy of the LST retrieval will be discussed in the next stage. (3) Although atmospheric profiles with different spatial resolutions have little impact on the retrieved LST (the difference in RMSE is less than 0.2 K) (Meng and Cheng 2018; Yang et al., 2020), an accurate atmospheric correction may be achieved by using the newly released ERA5 atmospheric profile, which has a high temporal resolution. (4) When validating LST products with ground observations, the reasonableness of pixels on the ground station should be explained. Although the heterogeneity of the SURF-RAD sites had been discussed in previous studies, the heterogeneity of the BSRN sites remains unknown. Additionally, more ground measurements under different water vapor content need to be collected, especially ground measurements under high water vapor content as future work.

6. LST mapping at the country level

We downloaded Landsat images of the Chinese landmass and continental United States for January and July. In total, we obtained 323 (248) and 966 (996) Landsat 5 images for January (July) 2005 in the Chinese landmass and continental United States, respectively; 444 (336) and 910 (953) Landsat 7 images for January (July) 2012 in the Chinese landmass and continental United States, respectively; and 551 (615) and 740 (939) Landsat 8 images for January (July) 2014 in the Chinese landmass and continental United States, respectively.

With the developed RTE method in Section 3, we retrieved the LSE and LST from these images. The monthly composited LST maps were derived from the retrieved LST by using the maximum value composition, which is shown in Figs. 15 and 16.

As shown in Figs. 15 and 16, we obtained the following results: (1) In both the United States and China, there was no significant spatial difference in LST in January, whereas the LST in July had large spatial variations. The LSTs in July were higher in both Northwest China and the western United States, which can be illustrated by the following reasons. Both Northwest China and the western United States are located in arid and semiarid regions, and the surface-atmosphere energy exchange is more direct without vegetation transpiration, which leads to higher LSTs.

(2) As seen from the monthly composite LST map, due to the effects of cloud contamination, the spatial coverage of LST maps is incomplete in both China and the United States, especially in southern China. As thermal infrared measurements are limited to cloud-free conditions due to their inability to penetrate clouds, the precipitation in southern China is high, and more cloud days occur in southern China; therefore, there are fewer valid Landsat images than in other regions. Moreover, the number of downloaded Landsat images is not the same, resulting in the
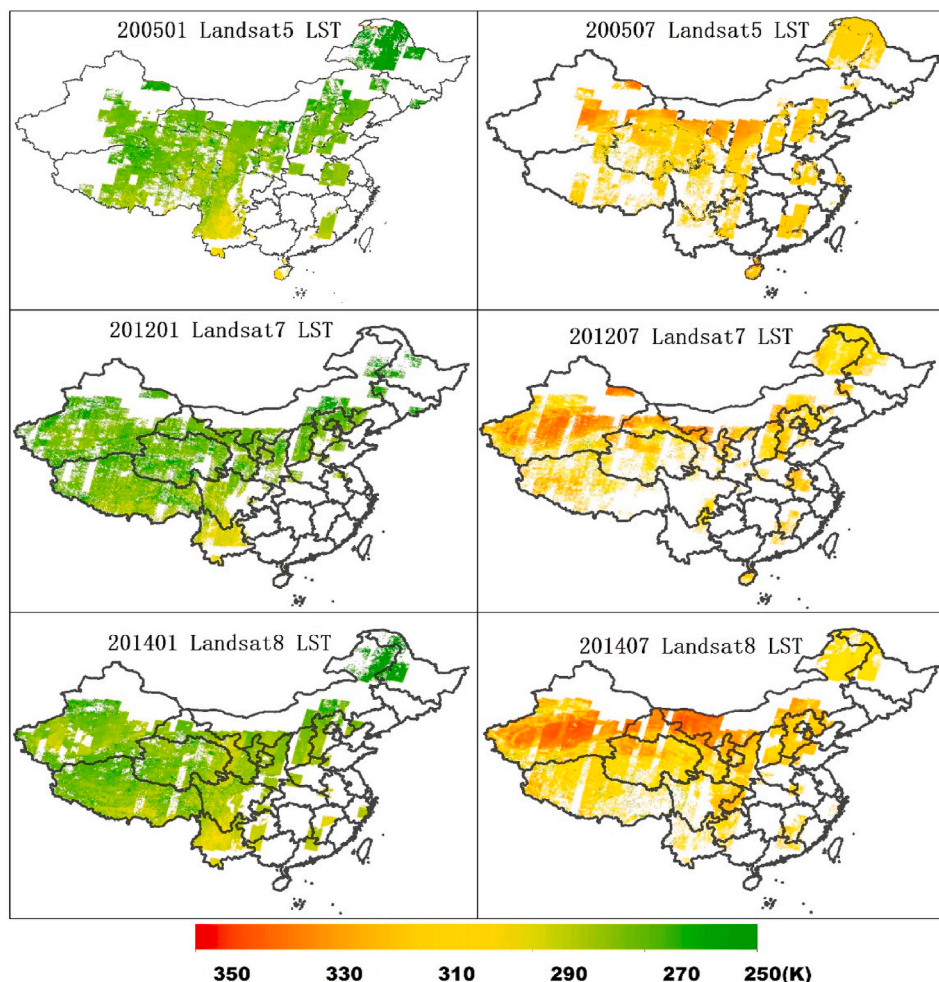

Fig. 15. Spatial distributions of the monthly LST maps composited from the retrieved Landsat 5, Landsat 7, and Landsat 8 LSTs in the Chinese landmass.
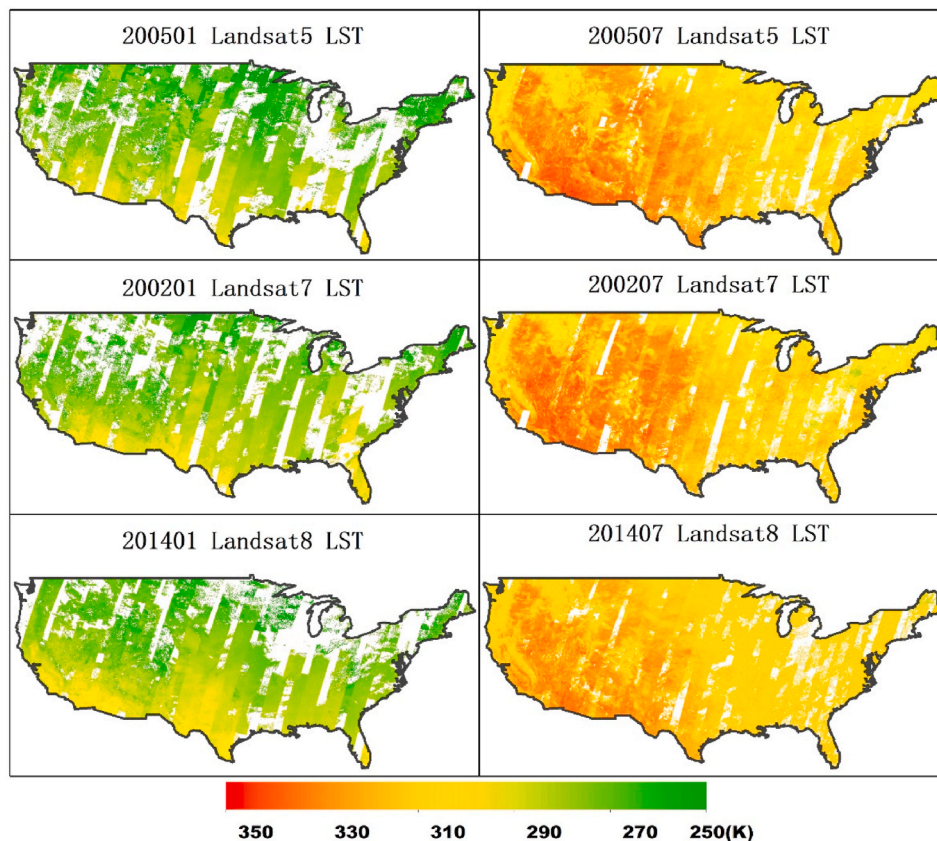
Fig. 16. Spatial distributions of the monthly LST maps composited from the retrieved Landsat 5, Landsat 7, and Landsat 8 LSTs in the continental United States.

different spatial coverage of the monthly composited LST maps.

7. Conclusion

Studies of water stress, fire monitoring, and evapotranspiration estimation at the field scale have a strong demand for long-time series, high spatial resolution LST products. In this study, we proposed an operational method to generate long-time series, 30-m land surface temperatures from Landsat series TIR observations. To achieve this goal, the radiative transfer equation (RTE)-based LST retrieval algorithm was chosen due to its clear physical mechanism and fewer assumptions. In the RTE-based LST retrieval algorithm, two core issues need to be resolved. The first is to determine the LSE. We propose a new scheme for estimating Landsat 5/7/8 LSE. The land surface was divided into four types: snow/ice, water, vegetated surface and nonvegetated surface. We developed specific methods for each type separately. The second is accurate atmospheric correction of TIR data, which relies on the accuracy of the selected atmospheric profile. The MERRA2 reanalysis product and RTTOV software were used for atmospheric correction based on extensive investigation. After addressing these two problems, LST was intuitively estimated by inverting the RTE.

Twenty-four ground LSE measurements collected from five sources and twelve ground LST measurements collected from global in situ sites were used to evaluate the estimated LSE on nonvegetated surfaces and the retrieved Landsat LST, respectively. The absolute mean bias of Landsat 5/7/8 LSE obtained by the new scheme is generally within 0.01, and the standard deviations are all less than 0.002. The average biases (RMSEs) at the SURFRAD sites are 1.11 (2.72), 1.54 (3.21), and 1.63 K (3.02 K) for Landsat 5, Landsat 7, and Landsat 8 LST, respectively, whereas the average biases (RMSEs) at the BSRN and Huailai sites are 0.08 (3.69) and 0.90 K (3.42 K) for Landsat 7 and Landsat 8, respectively. Compared with the USGS LST products, the LST estimated from

our method has higher accuracy, with biases (RMSEs) equal to 1.00 K (2.58 K),1.47 K (3.21 K), and 1.58 K (2.95 K) for our method and 1.68 K (3.50 K),1.11 K (3.53 K), and 1.55 K (3.52 K) for USGS LST. The abovementioned validation indicated that the Landsat LST product estimated from our method is at the first-class level, with a bias of ~1.5 K and an RMSE of ~3.0 K.

Furthermore, we retrieved Landsat LSTs of the Chinese landmass and continental United States with the developed RTE method and derived monthly composited LST maps by using the maximum value composition. Although the spatial coverage of the LST maps is incomplete due to the influence of clouds, the spatial distribution of the LST maps is reasonable. Combined with the validation results and the regional mapping at the country level, the operational method proposed in this paper is reliable and can be used for research on water stress, fire monitoring and evapotranspiration estimation. In the next stage, we will mass-produce global LSTs from Landsat series TIR data and release them to the public.

Declaration of competing interest

The authors declare that they have no known competing financial interests or personal relationships that could have appeared to influence the work reported in this paper.

Acknowledgement

References

Anderson, M.C., Allen, R.G., Morse, A., Kustas, W.P., 2012. Use of Landsat thermal imagery in monitoring evapotranspiration and managing water resources. Rem. Sens. Environ. 122, 50–65.

Baldridge, A.M., Hook, S.J., Grove, C.I., Rivera, G., 2009. The ASTER spectral library version 2.0. Rem. Sens. Environ. 113, 711–715.

Borel, C., 2008. Error analysis for a temperature and emissivity retrieval algorithm for hyperspectral imaging data. Int. J. Rem. Sens. 29, 5029–5045.

Chatterjee, R.S., Singh, N., Thapa, S., Sharma, D., Kumar, D., 2017. Retrieval of land surface temperature (LST) from landsat TM6 and TIRS data by single channel radiative transfer algorithm using satellite and ground-based inputs. Int. J. Appl. Earth Obs. Geoinf. 58, 264–277.

Chen, J.M., Cihlar, J., 1996. Retrieving leaf area index of boreal conifer forests using landsat TM images. Rem. Sens. Environ. 55, 153–162.

Cheng, J., Cheng, X., Meng, X., Zhou, G., 2019. A Monte Carlo emissivity model for wind-roughened sea surface. Sensors 19.

Cheng, J., Liang, S., 2014. Estimating the broadband longwave emissivity of global bare soil from the MODIS shortwave albedo product. J. Geophys. Res.: Atmospheres 119, 614–634.

Cheng, J., Liang, S., Dong, L., Ren, B., Shi, L., 2014a. Validation of the moderate-resolution imaging spectroradiometer land surface emissivity products over the Taklimakan Desert. J. Appl. Remote Sens. 8, 083675.

Cheng, J., Liang, S., Liu, H., Nie, A., Liu, Q., 2017a. A disaggregation approach for estimating high spatial resolution broadband emissivity for bare soils from Landsat surface reflectance. International Journal of Digital Earth 11, 691–702.

Cheng, J., Liang, S., Meng, X., Zhang, Q., Zhou, S., 2020. Chapter 7 - land surface temperature and thermal infrared emissivity. In: Liang, S., Wang, J. (Eds.), Advanced Remote Sensing, second ed. Academic Press, pp. 251–295.

Cheng, J., Liang, S., Nie, A., Liu, Q., 2017b. Is there a physical linkage between surface emissive and reflective variables over non-vegetated surfaces? Journal of the Indian Society of Remote Sensing 46, 591–596.

Cheng, J., Liang, S., Tzeng, Y.C., Dong, L., 2014b. Obtaining global land-surface broadband emissivity from MODIS collection 5 spectral albedos using a dynamic learning neural network. Int. J. Rem. Sens. 35, 1395–1416.

Cheng, J., Liang, S., Verhoef, W., Shi, L., Liu, Q., 2016. Estimating the hemispherical broadband longwave emissivity of global vegetated surfaces using a radiative transfer model. IEEE Trans. Geosci. Rem. Sens. 54, 905–917.

Cheng, J., Liang, S., Weng, F., Wang, J., Li, X., 2010. Comparison of radiative transfer models for simulating snow surface thermal infrared emissivity. IEEE Journal of Selected Topics in Applied Earth Observations and Remote Sensing 3, 323–336.

Cheng, J., Liang, S., Yao, Y., Zhang, X., 2013. Estimating the optimal broadband emissivity spectral range for calculating surface longwave net radiation. Geosci. Rem. Sens. Lett. IEEE 10, 401–405.

Cheng, J., Liu, H., Liang, S., Nie, A., Liu, Q., Guo, Y., 2017c. A framework for estimating the 30 m thermal-infrared broadband emissivity from Landsat surface reflectance data. J. Geophys. Res.: Atmospheres.

Coll, C., García-Santos, V., Niclòs, R., Caselles, V., 2016. Test of the MODIS land surface temperature and emissivity separation algorithm with ground measurements over a rice paddy. IEEE Trans. Geosci. Rem. Sens. 54, 3061–3069.

Cook, M., Schott, J., Mandel, J., Raqueno, N., 2014. Development of an operational calibration methodology for the landsat thermal data archive and initial testing of the atmospheric compensation component of a land surface temperature (LST) product from the archive. Rem. Sens. 6, 11244–11266.

Cristóbal, J., Jiménez-Muñoz, J., Prakash, A., Mattar, C., Skoković, D., Sobrino, J., 2018. An improved single-channel method to retrieve land surface temperature from the landsat-8 thermal band. Rem. Sens. 10, 431.

Cristóbal, J., Jiménez-Muñoz, J.C., Sobrino, J.A., Ninyerola, M., Pons, X., 2009. Improvements in land surface temperature retrieval from the Landsat series thermal band using water vapor and air temperature. J. Geophys. Res. 114.

Dhakar, R., Sehgal, V.K., Chakraborty, D., Sahoo, R.N., Mukherjee, J., 2019. Field scale wheat LAI retrieval from multispectral Sentinel 2A-MSI and LandSat 8-OLI imagery: effect of atmospheric correction, image resolutions and inversion techniques. Geocarto Int. 1–21.

Dong, L.X., Hu, J.Y., Tang, S.H., Min, M., 2013. Field validation of the GLASS land surface broadband emissivity database using pseudo-invariant sand dune sites in northern China. International Journal of Digital Earth 6, 96–112.

Duan, S.-B., Li, Z.-L., Li, H., Göttsche, F.-M., Wu, H., Zhao, W., Leng, P., Zhang, X., Coll, C., 2019. Validation of Collection 6 MODIS land surface temperature product using in situ measurements. Rem. Sens. Environ. 225, 16–29.

Duan, S.-B., Li, Z.-L., Zhao, W., Wu, P., Huang, C., Han, X.-J., Gao, M., Leng, P., Shang, G., 2020. Validation of Landsat land surface temperature product in the conterminous United States using in situ measurements from SURFRAD, ARM, and NDBC sites. International Journal of Digital Earth 1–21.

Eklundh, L., Harrie, L., Kuusk, A., 2001. Investigating relationships between Landsat ETM+ sensor data and leaf area index in a boreal conifer forest. Rem. Sens. Environ. 78, 239–251.

Emami, H., Mojaradi, B., Safari, A., 2016. A new approach for land surface emissivity estimation using LDCM data in semi-arid areas: exploitation of the ASTER spectral library data set. Int. J. Rem. Sens. 37, 5060–5085.

Ermida, S.L., Soares, P., Mantas, V., Göttsche, F.-M., Trigo, I.F., 2020. Google Earth engine open-source code for land surface temperature estimation from the landsat series. Rem. Sens. 12, 1471.

Fang, H., Liang, S., 2003. Retrieving leaf area index with a neural network method: simulation and validation. IEEE Trans. Geosci. Rem. Sens. 41, 2052–2062.

Ganguly, S., Nemani, R.R., Zhang, G., Hashimoto, H., Milesi, C., Michaelis, A., Wang, W., Votava, P., Samanta, A., Melton, F., Dungan, J.L., Vermote, E., Gao, F., Knyazikhin, Y., Myneni, R.B., 2012. Generating global leaf area index from landsat: algorithm formulation and demonstration. Rem. Sens. Environ. 122, 185–202.

García-Santos, V., Cuxart, J., Martínez-Villagrasa, D., Jiménez, M., Simó, G., 2018. Comparison of three methods for estimating land surface temperature from landsat 8-TIRS sensor data. Rem. Sens. 10, 1450.

Gillespie, A., Rokugawa, S., Matsunaga, T., Cothern, J.S., Hook, S., Kahle, A.B., 1998. A temperature and emissivity separation algorithm for advanced spaceborne thermal emission and reflection radiometer (ASTER) images. IEEE Trans. Geosci. Rem. Sens. 36, 1113–1126.

Gillespie, A.R., Abbott, E.A., Gilson, L., Hulley, G., Jiménez-Muñoz, J.-C., Sobrino, J.A., 2011. Residual errors in ASTER temperature and emissivity standard products AST08 and AST05. Rem. Sens. Environ. 115, 3681–3694.

Göttsche, F.-M., Olesen, F.-S., Bork-Unkelbach, A., 2013. Validation of land surface temperature derived from MSG/SEVIRI with in situ measurements at Gobabeb, Namibia. Int. J. Rem. Sens. 34, 3069–3083.

Griend, A.A.V.D., Owe, M., 1993. On the relationship between thermal emissivity and the normalized difference vegetation index for natural surfaces. Internatoinal Journal of Remote Sensing 14, 1119–1131.

Guillevic, P.C., Biard, J.C., Hulley, G.C., Privette, J.L., Hook, S.J., Olioso, A., Göttsche, F. M., Radocinski, R., Román, M.O., Yu, Y., Csiszar, I., 2014. Validation of land surface temperature products derived from the visible infrared imaging radiometer suite (VIIRS) using ground-based and heritage satellite measurements. Rem. Sens. Environ. 154, 19–37.

Hori, M., Aoki, T., Tanikawa, T., Motoyoshi, H., Hachikubo, A., Sugiura, K., Yasunari, T. J., Eide, H., Storvold, R., Nakajima, Y., Takahashi, F., 2006. In-situ measured spectral directional emissivity of snow and ice in the 8-14 um atmospheric window. Remote Sensing of Environmet 100, 486–502.

Hosgood, B., Jacquemoud, S., Andreoli, G., Verdebout, J., Pedrini, G., Schmuck, G., 1994. Leaf optical Properties EXperiment 93 (LOPEX93). In: Hosgood, B., Jacquemoud, S., Andreoli, G., Verdebout, J., Pedrini, G., Schmuck, G. (Eds.), *European Commission — Joint Research Center* (P. 095). Ispra (Italy): Inst. Remote Sensing Applications.

Hulley, G.C., Hook, S.J., 2009a. Intercomparison of versions 4, 4.1 and 5 of the MODIS Land Surface Temperature and Emissivity products and validation with laboratory measurements of sand samples from the Namib desert, Namibia. Rem. Sens. Environ. 113, 1313–1318.

Hulley, G.C., Hook, S.J., 2009b. the North American ASTER land surface emissivity database (NAALSED) version 2.0. Rem. Sens. Environ. 113, 1967–1975.

Hulley, G.C., Hook, S.J., Baldridge, A.M., 2009. Validation of the North American ASTER Land Surface Emissivity Database (NAALSED) version 2.0 using pseudo-invariant sand dune sites. Rem. Sens. Environ. 113, 2224–2233.

Jacquemoud, S., 1993. Inversion of the PROSPECT + SAIL canopy reflectance model from AVIRIS equivalent spectra theoretical study. Rem. Sens. Environ. 44, 281–292.

Jiménez-Muñoz, J.C., Cristobal, J., Sobrino, J.A., Soria, G., Ninyerola, M., Pons, X., Pons, X., 2009. Revision of the single-channel algorithm for land surface temperature retrieval from landsat thermal-infrared data. IEEE Trans. Geosci. Rem. Sens. 47, 339–349.

Jiménez-Muñoz, J.C., Sobrino, J.A., 2003. A generalized single-channel method for retrieving land surface temperature from remote sensing data. J. Geophys. Res. 108.

Jiménez-Muñoz, J.C., Sobrino, J.A., Skokovic, D., Mattar, C., Cristobal, J., 2014. Land surface temperature retrieval methods from landsat-8 thermal infrared sensor data. Geosci. Rem. Sens. Lett. IEEE 11, 1840–1843.

Jin, H., Li, A., Yin, G., Xiao, Z., Bian, J., Nan, X., Jing, J., 2019. A multiscale Assimilation approach to improve fine-resolution leaf area index dynamics. IEEE Trans. Geosci. Rem. Sens. 57, 8153–8168.

Kodimalar, T., Vidhya, R., Eswar, R., 2020. Land surface emissivity retrieval from multiple vegetation indices: a comparative study over India. Remote Sensing Letters 11, 176–185.

Li, H., Li, R., Yang, Y., Cao, B., Bian, Z., Hu, T., Du, Y., Sun, L., Liu, Q., 2020. Temperature-based and radiance-based validation of the collection 6 MYD11 and MYD21 land surface temperature products over barren surfaces in northwestern China. IEEE Trans. Geosci. Rem. Sens. 1–14.

Li, H., Sun, D., Yu, Y., Wang, H., Liu, Y., Liu, Q., Du, Y., Wang, H., Cao, B., 2014. Evaluation of the VIIRS and MODIS LST products in an arid area of Northwest China. Rem. Sens. Environ. 142, 111–121.

Li, S., Jiang, G.-M., 2018. Land surface temperature retrieval from landsat-8 data with the generalized split-window algorithm. IEEE Access 6, 18149–18162.

Li, Z.-L., Tang, B.-H., Wu, H., Ren, H., Yan, G., Wan, Z., Trigo, I.F., Sobrino, J.A., 2013a. Satellite-derived land surface temperature: current status and perspectives. Rem. Sens. Environ. 131, 14–37.

Li, Z.L., Tang, B.H., Wu, H., Ren, H., Yan, G., Wan, Z., Trigo, I.F., Sobrino, J.A., 2013b. Satellite-derived land surface temperature: current status and perspectives. Rem. Sens. Environ. 131, 14–37.

Liu, S.M., Xu, Z.W., Zhu, Z.L., Jia, Z.Z., Zhu, M.J., 2013. Measurements of evapotranspiration from eddy-covariance systems and large aperture scintillometers in the Hai River Basin, China. J. Hydrol. 487, 24–38.

Ma, M., Xiao, Q., 2017. HiWATER: Dataset of Thermal Infrared Spectrum Observed by BOMEM MR304 in the Middle Reaches of the Heihe River Basin. National Tibetan Plateau Data Center.

Malakar, N.K., Hulley, G.C., Hook, S.J., Laraby, K., Cook, M., Schott, J.R., 2018. An operational land surface temperature product for landsat thermal data: methodology and validation. IEEE Trans. Geosci. Rem. Sens. 56, 5717–5735.

Masek, J.G., Vermote, E.F., Saleous, N.E., Wolfe, R., Hall, F.G., Huemmrich, K.F., Gao, F., Kutler, J., Lim, T.K., 2006. A landsat surface reflectance dataset for North America, 1990–2000. Geosci. Rem. Sens. Lett. IEEE 3, 68–72.

Menenti, M., Bastiaanssen, W., Eick, D.v., Karim, M.A.A.e., 1989. Linear relationships between surface reflectance and temperature and their application to map actual evaporation of groundwater. Adv. Space Res. 9, 165–176.

Meng, X., Cheng, J., 2018. Evaluating eight global reanalysis products for atmospheric correction of thermal infrared sensor—application to landsat 8 TIRS10 data. Rem. Sens. 10, 474.

Meng, X., Cheng, J., 2020. Estimating land and sea surface temperature from cross-calibrated Chinese gaofen-5 thermal infrared data using split-window algorithm. Geosci. Rem. Sens. Lett. IEEE 17, 509–513.

Meng, X., Cheng, J., Liang, S., 2017. Estimating land surface temperature from feng Yun-3C/MERSI data using a new land surface emissivity scheme. Rem. Sens. 9, 1247.

Meng, X., Cheng, J., Zhao, S., Liu, S., Yao, Y., 2019. Estimating land surface temperature from landsat-8 data using the NOAA JPSS enterprise algorithm. Rem. Sens. 11, 155.

Niclòs, R., Galve, J.M., Valiente, J.A., Estrela, M.J., Coll, C., 2011. Accuracy assessment of land surface temperature retrievals from MSG2-SEVIRI data. Rem. Sens. Environ. 115, 2126–2140.

Ouyang, X., Chen, D., Lei, Y., 2018. A generalized evaluation scheme for comparing temperature products from satellite observations, numerical weather model, and ground measurements over the Tibetan plateau. IEEE Trans. Geosci. Rem. Sens. 56, 3876–3894.

Qin, Z., Karnieli, A., Berliner, P., 2001. A mono-window algorithm for retrieving land surface temperature from Landsat TM data and its application to the Israel-Egypt border region. Int. J. Rem. Sens. 22, 3719–3746.

Ren, H., Liu, R., Qin, Q., Fan, W., Yu, L., Du, C., 2017. Mapping finer-resolution land surface emissivity using Landsat images in China. J. Geophys. Res.: Atmospheres 122, 6764–6781.

Rosas, J., Houborg, R., McCabe, M.F., 2017. Sensitivity of landsat 8 surface temperature estimates to atmospheric profile data: a study using MODTRAN in dryland irrigated systems. Rem. Sens. 9, 988.

Rozenstein, O., Qin, Z., Derimian, Y., Karnieli, A., 2014. Derivation of land surface temperature for Landsat-8 TIRS using a split window algorithm. Sensors 14, 5768–5780.

Sabol Jr., D.E., Gillespie, A.R., Abbott, E., Yamada, G., 2009. Field validation of the ASTER temperature–emissivity separation algorithm. Rem. Sens. Environ. 113, 2328–2344.

Saradjian, M.R., Jouybari-Moghaddam, Y., 2019. Land Surface Emissivity and temperature retrieval from Landsat-8 satellite data using Support Vector Regression and weighted least squares approach. Remote Sensing Letters 10, 439–448.

Sekertekin, A., 2019. Validation of physical radiative transfer equation-based land surface temperature using landsat 8 satellite imagery and SURFRAD in-situ measurements. J. Atmos. Sol. Terr. Phys. 196.

Sekertekin, A., Bonafoni, S., 2020. Land surface temperature retrieval from landsat 5, 7, and 8 over rural areas: assessment of different retrieval algorithms and emissivity models and toolbox implementation. Rem. Sens. 12, 294.

Sobrino, J.A., Del Frate, F., Drusch, M., Jimenez-Munoz, J.C., Manunta, P., Regan, A., 2016. Review of thermal infrared applications and requirements for future high-resolution sensors. IEEE Trans. Geosci. Rem. Sens. 54, 2963–2972.

Sobrino, J.A., Jiménez-Muñoz, J.C., Paolini, L., 2004. Land surface temperature retrieval from LANDSAT TM 5. Rem. Sens. Environ. 90, 434–440.

Sobrino, J.A., Jimenez-Munoz, J.C., Soria, G., Romaguera, M., Guanter, L., Moreno, J., Plaza, A., Martinez, P., 2008. Land surface emissivity retrieval from different VNIR and TIR sensors. IEEE Trans. Geosci. Rem. Sens. 46, 316–327.

Sobrino, J.A., Jiménez-Muñoz, J.C., Sòria, G., Gómez, M., Ortiz, A.B., Romaguera, M., Zaragoza, M., Julien, Y., Cuenca, J., Atitar, M., Hidalgo, V., Franch, B., Mattar, C., Ruescas, A., Morales, L., Gillespie, A., Balick, L., Su, Z., Nerry, F., Peres, L., Libonati, R., 2010. Thermal remote sensing in the framework of the SEN2FLEX project: field measurements, airborne data and applications. Int. J. Rem. Sens. 29, 4961–4991.

Sobrino, J.A., Raissouni, N., 2000. Toward remote sensing methods for land cover dynamic monitoring: application to Morocco. Int. J. Rem. Sens. 21, 353–366.

Sulla-Menashe, D., Gray, J.M., Abercrombie, S.P., Friedl, M.A., 2019. Hierarchical mapping of annual global land cover 2001 to present: the MODIS Collection 6 Land Cover product. Rem. Sens. Environ. 222, 183–194.

Tang, B.H., Shao, K., Li, Z.L., Wu, H., Tang, R., 2015. An improved NDVI-based threshold method for estimating land surface emissivity using MODIS satellite data. Int. J. Rem. Sens. 36, 4864–4878.

Tang, B.H., Zhan, C., Li, Z.L., Hua, W., Tang, R., 2017. Estimation of land surface temperature from MODIS data for the atmosphere with air temperature inversion profile. IEEE Journal of Selected Topics in Applied Earth Observations and Remote Sensing 10, 2976–2983.

Trigo, I.F., Monteiro, I.T., Olesen, F., Kabsch, E., 2008. An assessment of remotely sensed land surface temperature. J. Geophys. Res. 113 https://doi.org/10.1029/2008JD010035.

Vanhellemont, Q., 2020. Combined land surface emissivity and temperature estimation from Landsat 8 OLI and TIRS. ISPRS J. Photogrammetry Remote Sens. 166, 390–402.

Verhoef, W., Jia, L., Xiao, Q., Su, Z., 2007. Unified optical-thermal four-stream radiative transfer theory for homogeneous vegetation canopies. IEEE Trans. Geosci. Rem. Sens. 45, 1808–1822.

Vermote, E., Justice, C., Claverie, M., Franch, B., 2016. Preliminary analysis of the performance of the Landsat 8/OLI land surface reflectance product. Rem. Sens. Environ. 185, 46–56.

Wan, Z., 2014. New refinements and validation of the collection-6 MODIS land-surface temperature/emissivity product. Rem. Sens. Environ. 140, 36–45.

Wan, Z., Dozier, J., 1996. A generalized split-window algorithm for retrieving land-surface temperature from space. IEEE Trans. Geosci. Rem. Sens. 34, 892–905.

Wang, F., Qin, Z., Song, C., Tu, L., Karnieli, A., Zhao, S., 2015a. An improved mono-window algorithm for land surface temperature retrieval from landsat 8 thermal infrared sensor data. Rem. Sens. 7, 4268–4289.

Wang, H., Xiao, Q., Li, H., Du, Y., Liu, Q., 2015b. Investigating the impact of soil moisture on thermal infrared emissivity using ASTER data. Geosci. Rem. Sens. Lett. IEEE 12, 294–298.

Wang, H., Yu, Y., Yu, P., Liu, Y., 2020. Land surface emissivity product for NOAA JPSS and GOES-R missions: methodology and evaluation. IEEE Trans. Geosci. Rem. Sens. 58, 307–318.

Wang, J., Xiao, X., Bajgain, R., Starks, P., Steiner, J., Doughty, R.B., Chang, Q., 2019. Estimating leaf area index and aboveground biomass of grazing pastures using Sentinel-1, Sentinel-2 and Landsat images. ISPRS J. Photogrammetry Remote Sens. 154, 189–201.

Wang, M., Zhang, Z., Hu, T., Wang, G., He, G., Zhang, Z., Li, H., Wu, Z., Liu, X., 2020. An efficient framework for producing landsat-based land surface temperature data using google Earth engine. IEEE Journal of Selected Topics in Applied Earth Observations and Remote Sensing 13, 4689–4701.

Windahl, E., Beurs, K.d., 2016. An intercomparison of Landsat land surface temperature retrieval methods under variable atmospheric conditions using in situ skin temperature. Int. J. Appl. Earth Obs. Geoinf. 51, 11–27.

Wu, X., Smith, W.L., 1997. Emissivity of rough sea surface for 8-13 um: modeling and verification. Appl. Opt. 36, 2609–2619.

Wulder, M.A., Loveland, T.R., Roy, D.P., Crawford, C.J., Masek, J.G., Woodcock, C.E., Allen, R.G., Anderson, M.C., Belward, A.S., Cohen, W.B., Dwyer, J., Erb, A., Gao, F., Griffiths, P., Helder, D., Hermosilla, T., Hipple, J.D., Hostert, P., Hughes, M.J., Huntington, J., Johnson, D.M., Kennedy, R., Kilic, A., Li, Z., Lymburner, L., McCorkel, J., Pahlevan, N., Scambos, T.A., Schaaf, C., Schott, J.R., Sheng, Y., Storey, J., Vermote, E., Vogelmann, J., White, J.C., Wynne, R.H., Zhu, Z., 2019. Current status of Landsat program, science, and applications. Rem. Sens. Environ. 225, 127–147.

Wulder, M.A., White, J.C., Loveland, T.R., Woodcock, C.E., Belward, A.S., Cohen, W.B., Fosnight, E.A., Shaw, J., Masek, J.G., Roy, D.P., 2016. The global Landsat archive: status, consolidation, and direction. Rem. Sens. Environ. 185, 271–283.

Xu, S., Cheng, J., 2021. A new land surface temperature fusion strategy based on cumulative distribution function matching and multiresolution Kalman filtering. Rem. Sens. Environ. 254, 112256.

Yang, J., Duan, S.-B., Zhang, X., Wu, P., Huang, C., Leng, P., Gao, M., 2020. Evaluation of seven atmospheric profiles from reanalysis and satellite-derived products: implication for single-channel land surface temperature retrieval. Rem. Sens. 12, 791.

Yu, X., Guo, X., Wu, Z., 2014. Land surface temperature retrieval from landsat 8 TIRS—comparison between radiative transfer equation-based method, split window algorithm and single channel method. Rem. Sens. 6, 9829–9852.

Yu, Y., Privette, J.L., Pinheiro, A.C., 2005. Analysis of the NPOESS VIIRS land surface temperature algorithm using MODIS data. IEEE Trans. Geosci. Rem. Sens. 43, 2340–2350.

Yu, Y., Tarpley, D., Privette, J.L., Goldberg, M.D., Raja, M.K.R.V., Vinnikov, K.Y., Xu, H., 2009. Developing algorithm for operational GOES-R land surface temperature product. IEEE Trans. Geosci. Rem. Sens. 47, 936–951.

Zeng, Q., Cheng, J., Dong, L., 2020. Assessment of the long-term high-spatial resolution Global LAnd Surface Satellite (GLASS) surface longwave radiation product using ground measurements. IEEE Journal of Selected Topics in Applied Earth Observations and Remote Sensing 13, 2032–2055.

Zhang, B., Zhang, M., Hong, D., 2019. Land Surface Temperature Retrieval from Landsat 8 OLI/TIRS Images Based on Back-Propagation Neural Network. Indoor and Built Environment, 1420326X1988207.

Zhang, Q., Cheng, J., 2020. An empirical algorithm for retrieving land surface temperature from AMSR-E data considering the comprehensive effects of environmental variables. Earth and Space Science 7.

Zhou, J., Li, J., Zhang, L., Hu, D., Zhan, W., 2011. Intercomparison of methods for estimating land surface temperature from a Landsat-5 TM image in an arid region with low water vapour in the atmosphere. Int. J. Rem. Sens. 33, 2582–2602.

Zhou, J., Zhan, W., Hu, D., Zhao, X., 2010. Improvement of mono-window algorithm for retrieving land surface temperature from HJ-1B satellite data. Chin. Geogr. Sci. 20, 123–131.

Zhang, Z., He, G., Wang, M., Long, T., Wang, G., Zhang, X., 2016. Validation of the generalized single-channel algorithm using Landsat 8 imagery and SURFRAD ground measurements. Remote Sensing Letters 7, 810–816.